Revealing a hidden conducting state by manipulating the intracellular domains in K_V10.1 exposes the coupling between two gating mechanisms.

Reham Abdelaziz[1], Adam P. Tomczak[1], Andreas Neef[2]* and Luis A. Pardo[1]*

[1]Oncophysiology Group. Max Planck Institute for Multidisciplinary Sciences, City Campus.

[2]Neurophysics Laboratory. Göttingen Campus Institute for Dynamics of Biological Networks.

Abstract

The *KCNH* family of potassium channels serves relevant physiological functions in both excitable and non-excitable cells, reflected in the massive consequences of mutations or pharmacological manipulation of their function. This group of channels shares structural homology with other voltage-gated K^+ channels. Still, the mechanisms of gating in this family show significant differences with respect to the canonical electromechanical coupling in these molecules. In particular, the large intracellular domains of *KCNH* channels play a crucial role in gating that is still only partly understood. Using *KCNH1*(K_V10.1) as a model, we have characterized the behavior of a series of modified channels that the current models could not explain. With electrophysiological and biochemical methods combined with mathematical modeling, we show that the behavior of the mutants can be explained by the uncovering of an open state that is not detectable in the wild type, is accessed from deep closed states, and reflects an intermediate step along the chain of events leading to channel opening. This allowed us to study gating steps prior to opening, which, for example, explain the mechanism of gating inhibition by Ca^{2+}-Calmodulin, and generate a gating model that describes the characteristic features of *KCNH* channels gating.

Introduction

Voltage-gated potassium channels constitute a large family of proteins that allow K^+ flow upon changes in the membrane potential. Their general architecture consists of a tetrameric complex with six transmembrane segments (S1-S6) in each subunit to form a central pore with four voltage sensors at the periphery. S1 to S4 segments constitute the sensor domain, while S5 and S6 segments and the loop between them line the pore. The mechanism of voltage-dependent gating is well understood for several subfamilies, namely those closely related to the *Drosophila Shaker* channel (*KCNA* and *KCNB*). In this subset of families, the linker between the sensor and pore domains (S4-S5 linker) acts as a mechanical lever transferring the movement of the voltage sensor to the gate at the bottom of S6 in a neighboring subunit through physical interaction (Barros et al., 2020). Such trans-subunit interaction is commonly denoted "domain swapping." In other families, gating mechanics must be different because there is no domain swapping in the transmembrane regions. Such is the case of the EAG family (*KCNH*) (Tomczak et al., 2017;Malak et al., 2019;Whicher and MacKinnon, 2019), whose members are implicated in many pathological conditions (Bauer and Schwarz, 2018;Toplak et al., 2022), which makes them attractive therapeutic targets.

In the *KCNH* channel family, sensor-to-pore coupling does not follow the conventional model; *KCNH* channels do not display domain-swapping in the transmembrane domains, the S4-S5 segment is very short and does not form a helix (Whicher and MacKinnon, 2016;Wang and MacKinnon, 2017) and voltage-dependent gating in $K_V10.1$ (Lörinczi et al., 2015) or $K_V11.1$ (de la Pena et al., 2018) occurs even when the S4-S5 linker is severed or removed. *KCNH* channels show extensive conserved intracellular domains. The eag domain in the N-terminus, formed by the PAS domain and PAS-Cap, interacts with the CNBHD (cyclic nucleotide-binding homology domain) of the neighboring subunit, which is connected to the S6 through the C-linker, see Fig. S1A). The four eag-CNBHD complexes form a ring in the intracellular side of the channel, connected to the gate via the C-linkers (Whicher and MacKinnon, 2016;Whicher and MacKinnon, 2019). Thus, there is domain-swapping within intracellular domains instead of the transmembrane segments (reviewed e.g., in (Barros et al., 2020;Codding et al., 2020)). This arrangement makes the intracellular ring an excellent candidate to participate in the gating process, as it has been demonstrated for other channels, e.g. (James and Zagotta, 2017;Codding et al., 2020;Nunez et al., 2020;Verkest et al., 2022). Indeed, gating of *KCNH* channels is affected by manipulations of either the eag domain, the CNBHD, or the interaction between them (Terlau et al., 1997;Ju and Wray, 2006;Sahoo et al., 2012;Gianulis et al., 2013;Dai and Zagotta, 2017;Dai et al., 2018;Codding and Trudeau, 2019;Malak et al., 2019;Whicher and MacKinnon, 2019;Codding et al., 2020). Furthermore, the stability of the interaction between PAS domain and C-terminus is altered by gating in KCNH2 channels (Harley et al., 2021). Recent Cryo-EM work revealed that the position of the voltage sensor in an electric field would preclude the opening of the gate (Mandala and

MacKinnon, 2022). After reliving such an obstacle upon depolarization, a rotation of the intracellular ring would allow the helices at the bottom of S6 to dilate, opening the gate (Wynia-Smith et al., 2008;Thouta et al., 2014;Whicher and MacKinnon, 2016;Wang and MacKinnon, 2017;Whicher and MacKinnon, 2019). Moreover, cryo-EM data on $K_V10.2$ (which shows 76% identity with $K_V10.1$) reveals a pre-open state in which the transmembrane regions of the channel are compatible with ion permeation, but is still a non-conducting state (Tian et al., 2023).

The behavior of the intracellular ring is also subject to modulation by different factors. For example, ligand binding to the PAS domain can also modify gating (Wang et al., 2020). The association of $K_V10.1$ with calmodulin (CaM), which in the presence of Ca^{2+} efficiently inhibits the channel, adds an additional level of complexity (Schonherr et al., 2000;Whicher and MacKinnon, 2016). $K_V10.1$ has CaM binding sites at the N- and the C-termini (Ziechner et al., 2006;Gonçalves and Stühmer, 2010). CaM presents two lobes (N- and C-lobe) that bind Ca^{2+} and a flexible helix in between. The N-lobe of CaM (Babu et al., 1985) binds to the N-site in the channel, while the C-lobe binds the C-terminal sites of an opposite subunit (Whicher and MacKinnon, 2016). This represents a cross-linking of two segments of the ring that possibly impairs its rotation and can thus be the basis of the inhibitory action of CaM through modulating the intracellular ring.

Yet, the mechanism coupling the movement of the sensor and the rotation of the ring remains unsolved. Importantly, mutations in both the intracellular N- (Whicher and MacKinnon, 2019) and C-terminal domains cause unexpected rectification (Zhao et al., 2017) or paradoxical activation by Ca-CaM instead of the normal inhibition seen in wild type (Lörinczi et al., 2016). In this study, we provide a mechanistic explanation of the hallmarks of $K_V10.1$ gating and define the role of the intracellular ring using a combination of electrophysiology and mutagenesis, modeling, and biochemical approaches. Channel variants with altered interaction between PASCap and CNBHD uncovered an open state in the mutants, different from the main open state in the wild type, with higher conductance. This made the transition between the voltage sensor movement and the ring rotation visible, allowing the characterization of gating steps hidden in the wild type. The novel open state can be best accessed from deep closed states (strong hyperpolarized membrane potential) and is promoted by binding of CaM, thus explaining the paradoxical effects of CaM in mutant channels. We propose a model tightly constrained by data that can explain the main differential features of $K_V10.1$ gating.

Results

Disrupting the interaction between PASCap and CNBHD reveals a biphasic gating behavior.

The first N-terminal residues of $K_V10.1$ are prime candidates for the transmission of voltage sensor motion to the intracellular domain based on crystal structures and interactions inferred from mutant function. In particular, two residues at the bottom of S4 (H343 (Terlau et al., 1997) and D342 (Tomczak et al., 2017)} functionally interact with the initial N-terminus. The N-terminal PAS domain can then transmit mechanical cues to its C-terminal interaction partner CNBHD (Whicher and MacKinnon, 2016;Codding and Trudeau, 2019;Whicher and MacKinnon, 2019;Codding et al., 2020;Wang et al., 2020;Mandala and MacKinnon, 2022). To study $K_V10.1$ gating under perturbed intramolecular interaction, we deleted the PASCap domain (residues 2-25) and, in a more conservative approach, we examined the impact of a point mutation (E600R) reported to disrupt the PASCap-CNBHD interaction (Haitin et al., 2013). We then obtained the response of the mutants to discrete depolarizations to different potentials (-100 to +120 mV for 300ms) in *Xenopus* oocytes in the presence of 60 mM K^+ in the extracellular solution to follow deactivation behavior through tail currents.

Fig. 1A displays representative current traces of WT and the mutant channels. The threshold for activation was shifted towards hyperpolarizing values in both mutants, giving rise to inward currents at potentials that do not lead to the opening of WT channels. This is most obvious in the biphasic conductance-voltage (GV) plots (Fig. 1B). The kinetics of activation (Fig. 1C) and deactivation (Fig 1E) of the mutants were also clearly distinguishable from WT. To facilitate the description of the results, we classified the responses into three categories depending on the stimulus amplitude: *weak* (-90mV to -20mV), *moderate* (-10mV to +40mV), and *strong* (+50 to +120mV).

While the activation of WT currents does not accelerate dramatically with increasing depolarizations in the voltage range tested, the mutants activated much slower than the WT upon *weak* and *moderate* depolarizations, reaching activation kinetics similar to WT with *strong* ones, as can be observed in normalized traces (Fig 1C). To obtain a more quantitative estimation of the changes in activation velocity, we used the time required to reach 80% of the maximum current amplitude plotted against the stimulus voltage (Fig. 1D). ΔPASCap and E600R needed a much longer time than WT to activate at *weak* depolarizing potentials but were equally fast at membrane potentials larger than +50 mV.

The deactivation (tail) kinetics changes with increasing depolarizations were more evident and more complex than changes in activation kinetics (Fig. 1E and 1F). For increasing test pulse potentials, the peak amplitude of ΔPASCap tail currents first increased progressively, then decreased at *moderate* values, and

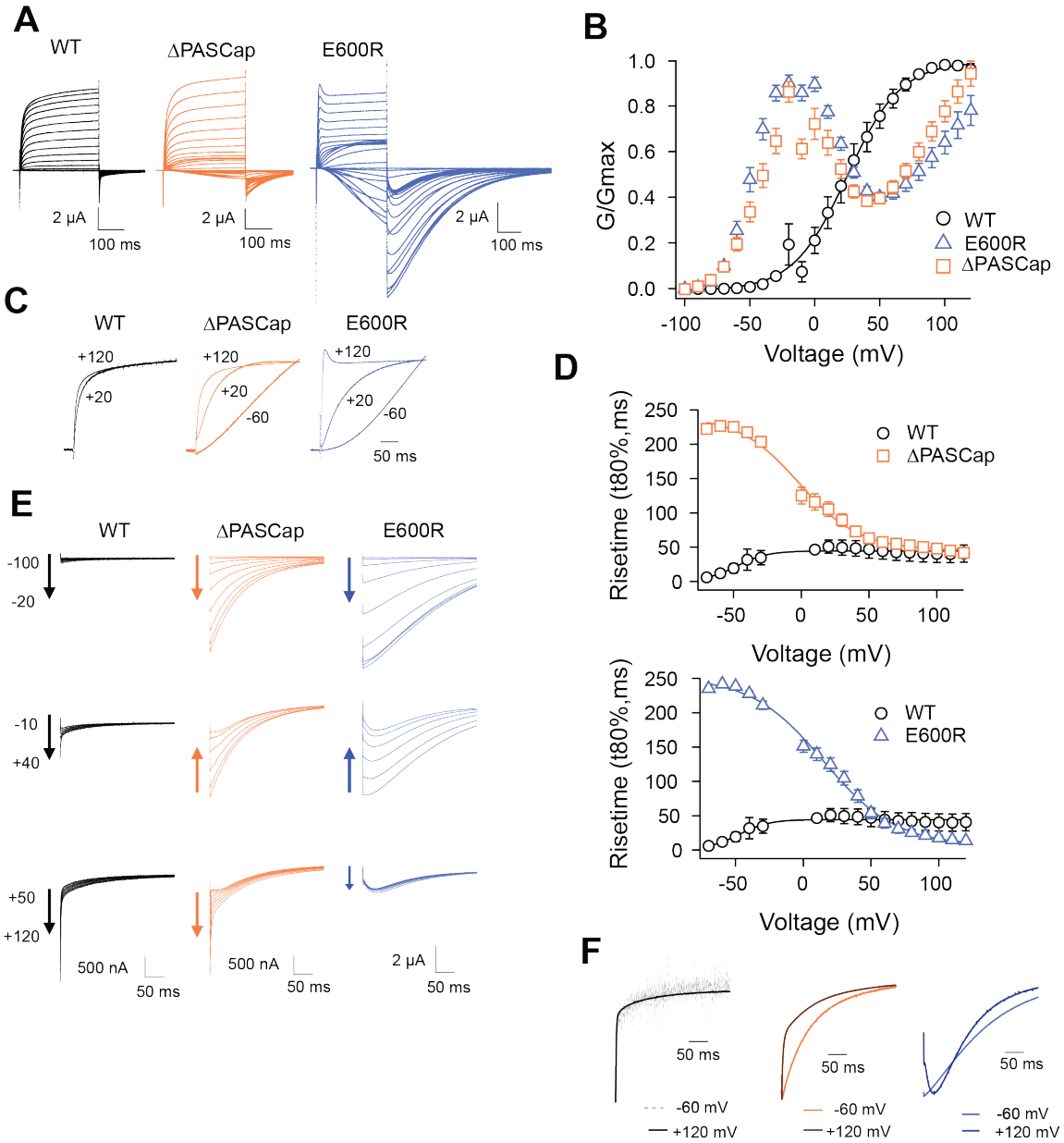

Figure 1. Characterization of ΔPASCap and E600R mutants. A. Raw current traces resulting from depolarizations between -100 and +120mV in WT (black), ΔPASCap (orange) and E600R (blue). **B**. GV plots corresponding to the three channel variants (colors as in A). (N: WT = 6, ΔPASCap = 7, E600R = 11; mean±SEM) **C**. Normalized traces to the indicated voltages to reveal the acceleration of activation with depolarization in the mutants. WT does not activate at -60mV type. **D**. Rise time of ΔPASCap (up) and E600R (down) as a function of voltage. The activation is much slower than in WT up to +50mV but reaches the speed of WT with stronger stimuli. **E**. Tail currents at -100 mV after depolarizations to potentials in the weak, medium, or strong range (up to down, see text for details). The arrows indicate the direction of the change in tail peak amplitude with increasing voltage. **F**. Normalized tail currents at -100 mV after depolarizations to the indicated voltages.

rose again after the range of *strong* depolarizations. E600R showed a similar pattern of tail amplitude, although the increase at *strong* potentials was less pronounced. Remarkably, both the tail amplitude and its

decay kinetics underwent profound changes depending on the stimulus. While the kinetics of WT tail currents was the same across different potentials, showing the characteristically fast deactivation of $K_V10.1$, ΔPASCap deactivated slow- and monotonically at *weak* depolarizations, but a fast component started to become evident after *moderate* stimuli. The fast component dominated the process at *strong* depolarizations. For E600R, the deactivation after *weak* stimuli was also slow and accelerated after a rising phase in the *moderate* and *strong* depolarization range.

Due to the complex behavior of the tail currents, different equations would be needed to fit the tails of the various channels to extrapolate the amplitude to time zero. Hence, to calculate the conductance, we simply used the current amplitude at the end of the stimulus and divided it by the driving force calculated from the reversal potential (Fig. 1B). As already observed in the raw traces, the threshold for activation for both mutants was strongly shifted in the hyperpolarizing direction with respect to WT (-80mV *vs.* -20mV). Still, the most evident change was that both ΔPASCap and E600R displayed a biphasic GV in contrast to WT. *Weak* depolarizing pulses increased the conductance of both mutants until a maximum at approximately +10mV. With further depolarizations, the conductance initially declined to rise again in response to *strong* depolarizations. This finding matches the changes in amplitude of the tail currents, which, therefore, probably reflect a true change in conductance. A similar behavior had been mentioned for related (Whicher and MacKinnon, 2019) or unrelated mutations (Zhao et al., 2017) affecting the intracellular domains. However, the reasons for this phenomenon had not been investigated. We thus aimed to understand the molecular mechanisms underlying the biphasic GV.

The biphasic GV is described by two sigmoidal components corresponding to a two-step gating mechanism.

One possible explanation for the biphasic behavior could be the coexistence of two separate channel populations with different kinetics, conductance, and voltage dependence. This seems unlikely because the shape of the GVs was consistent in all our recordings, as evidenced by the small error bars (Fig. 1B) despite the variability intrinsic to the oocyte system. Alternatively, each channel could have two open states, and the rectification observed between the two conductance components represents a transition from one state to the other. Indeed, an equation that reflects the two components and a transition between them (see Methods) described the behavior of the GV of both mutants accurately (Fig. 2A).

With the available structural information in mind, the two components could represent sequential access to two open states (from here on, O_1 and O_2) through two gating steps that differentially involve the sensor

movement and ring rotation (Tomczak et al., 2017;Whicher and MacKinnon, 2019;Mandala and MacKinnon, 2022).

To test if the ring underlies one of the two gating steps, we tested the behavior of additional N-terminal deletions of increasing length (Δ2-10, 2-25 for ΔPASCap, and 2-135 for Δeag), expected to disrupt the ring integrity more and more. A biphasic GV was observed in all these mutants (Fig. 2A). The V_{half} value of the first component was very similar across mutants. In contrast, the second component showed different thresholds. We then performed a global fit using equation 4, where we linked the parameters of the first components (Vh_1, K_1) across mutants and allowed the parameters for the second component (Vh_2, K_2, A_2) and the transition (Vh_3, K_3) to vary (Table S1, Fig. 2B). The global fit accurately described the behavior of the GV in all mutants (Fig. 2A).

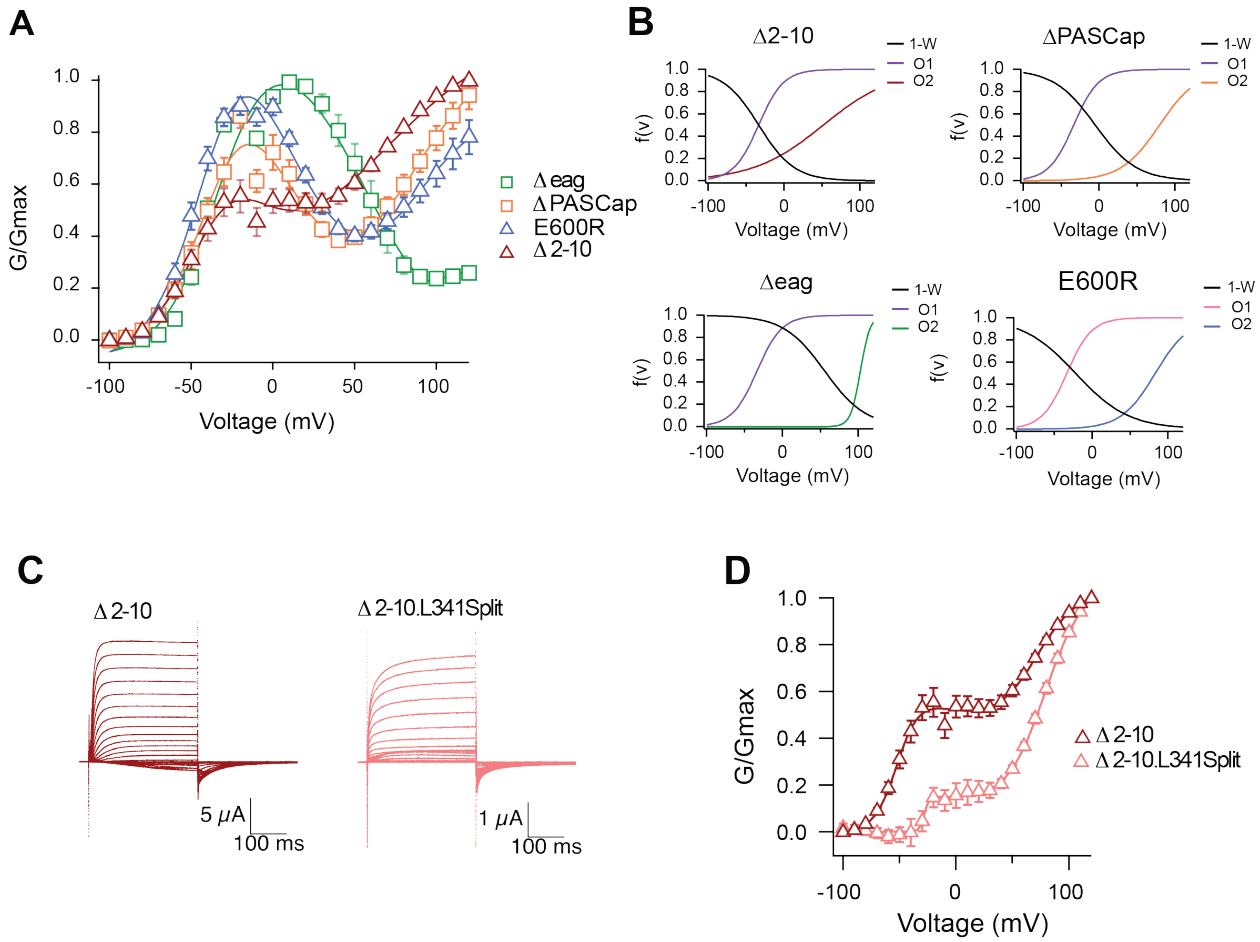

Figure 2. The biphasic GV corresponds to two sequential events. A. The GV of all tested mutants show biphasic behavior. (N: Δ2-10 = 6, ΔPASCap = 7, Δeag = 7, E600R = 11; mean±SEM). All are well described by *Eq. 4* in a global fit with fixed parameters for the first component. **B**. Distribution of the three components used for the fits as a function of voltage. **C**.A discontinuous form of Δ2-10 shows attenuated biphasic behavior. **D**. GV plots of Δ2-10 and Δ2-10.L341Split (N: Δ2-10 = 6, Δ2-10.L341Split = 5; ±SEM). Split fitted using *Eq. 4*.

	Δ2-10	ΔPASCap	Δeag	E600R
A_0	-0.052	-0.054	-0.067	-0.091
A_1	1.78	1.78	1.32	2.99
Vh_1	-33.57	-33.57	-33.57	-33.57
K_1	16.38	16.38	16.38	16.38
A_2	1.31	1.18	0.25	0.99
Vh_2	51.63	79.63	102.70	83.04
K_2	46.05	25.38	6.41	22.51
Vh_3	-33.47	-5.16	55.52	-21.93
K_3	23.47	27.12	27.01	34.9

Table S1. Parameters of a global fit that linked the first component of the biphasic response

The result of the global fit indicates that the first component is conserved across mutants. In contrast, the second component occurs at progressively more depolarized potentials for increasingly larger N-terminal deletions. Thus, the underlying gating events can be separated into two steps: A first gating step of the voltage sensor, which affects opening without engaging the ring and leads to a non-conducting pre-open state in the WT which is conducting in our mutants, and a second gating event, operating at higher depolarizations, that involves a change in the ring.

To test this hypothesis, we compared the behavior of Δ2-10 and Δ2-10.L341Split, a channel lacking a covalent connection between the sensor and the pore domain (Tomczak et al., 2017) hence decoupling residues downstream S4 (in this case starting from 342) from the movement of the sensor. As predicted, compared to Δ2-10, Δ2-10.L341Split showed a significant reduction in the first component of the biphasic GV (Fig. 2C, D).

Activation of WT $K_V10.1$ channels (best studied for the *Drosophila* form *eag*) drastically slows down in the presence of extracellular divalent cations that bind to the voltage sensor (Silverman et al., 2000;Tang et al., 2000), e.g., Mg^{2+}, Ni^{2+}, Co^{2+}, and Mn^{2+}, but not Ca^{2+}. Strikingly, the degree of deceleration correlates with the ions' hydration enthalpy, suggesting that the ion might unbind during activation (Terlau et al., 1996). In addition, deep deactivated states are accessed with less hyperpolarization when these divalents are present. We chose to study the impact of Mg^{2+} on the kinetics and voltage dependence of activation (Fig. 3) in the mutant Δeag, which shows the most significant separation between the two conductance components. Mg^{2+} slowed the activation of the channel at all depolarizations, affecting entry to both open states. This result suggests that Mg^{2+} also slows the voltage sensor motion that controls access into the second open state. In addition, the voltage dependence of activation was shifted by approximately 25 mV to more depolarized voltages. This is in line with Mg^{2+} promoting access to deep deactivated states requiring

stronger depolarization to exit them. Interestingly, the transition from the first to the second component of the GV plot seems unaffected by the divalent binding.

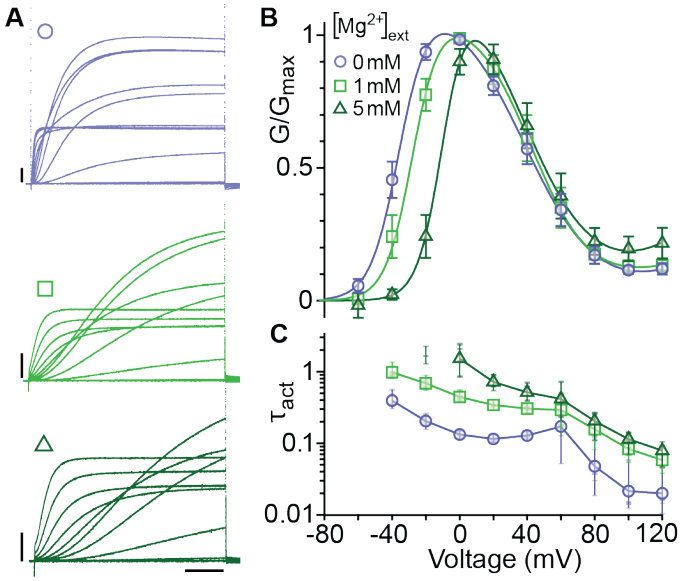

Figure 3. Mg^{2+} induces a shift of the first component in the depolarizing direction. A. Raw current traces from oocytes expressing Δeag channels in response to depolarizations from a holding potential of -100 mV to voltages between -100 and +120 mV in the presence of 0, 1 or 5 mM $MgCl_2$ in the external solution (legend in B). Scale bars are 1µA and 200 ms. **B**. Average GV plots (with SEM) obtained under the same conditions from n=6, 6, and 5 recordings (0, 1, and 5 mM $MgCl_2$). The V_{half} of the first component shifts from -35.8 mV in the absence of extracellular Mg^{2+} to -27.9 and -9.9 mV in 1 mM and 5 mM $MgCl_2$. **C**. Time constants of the early activation show decelerating effect of Mg^{2+}. Symbols depict averages, vertical lines the range and horizontal lines individual experiments. For voltages, where conductances or time constants could not be reasonably estimated no data are displayed.

Steady-state voltage dependence and activation kinetics are consistent with two open states (O_1 and O_2) with different conductance.

Thus far, our results are compatible with two different open states in the mutants. The first open state, the mutant-specific O_1, would dominate at *weak* depolarizations and deactivate slowly, with tail current decay

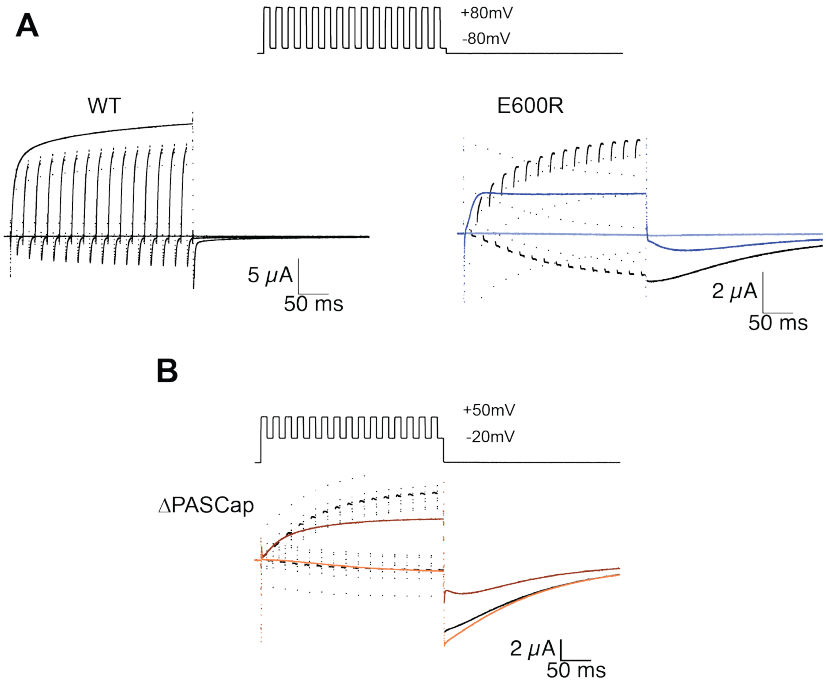

Figure 4. Alternating stimuli reveal larger conductance for O_1. A. Alternating potential between -80 and 80 mV in the WT results in current amplitudes that are smaller than those during a sustained stimulus (Upper left traces). In contrast, E600R gave rise to larger currents when the stimulus was intermittent and too short to allow occupancy of O_2 (upper right). **B**. The effect was qualitatively similar for ΔPASCap, which consistently gave rise to larger current upon oscillating stimuli between -20 and +50 mV than during a constant pulse to +50 mV.

time constants of tens of milliseconds. In contrast, mutant and WT channels would reach the second open state (O_2) at strong depolarizations and deactivate more rapidly, with a few milliseconds or less time constants. A critical test of this hypothesis is the application of more complex voltage stimuli that drive the system to a non-equilibrium state of high O_1 occupancy. This might be achieved by deactivation periods of around 10 ms, just long enough to remove most channels from O_2 but sufficiently brief to maintain the occupancy of O_1. For simplicity, we used depolarization periods of the same duration and tested whether a 300 ms series of activating and deactivating 10 ms pulses could accumulate channels in a high conductance state O_1.

For WT (Fig. 4A), alternating between -80 and +80 mV resulted in a smaller amplitude than a constant stimulus to +80 mV, just as expected for a system with a single open state and a monotonic voltage dependence of activation. What is more, the rapid deactivation of WT resulted in near-complete deactivation during every cycle.

In E600R, in contrast, the current amplitude during activating pulses increased steadily from cycle to cycle. Ultimately the current amplitude exceeds that obtained with a constant +80mV pulse (Fig. 4A). Because the deactivation of this mutant is much slower and occurs at more negative potentials than that of WT (see Fig. 1 and 2B), there was no noticeable deactivation during the -80 mV episodes. In addition, the tail current after the alternating stimuli had a larger amplitude than the one after a continuous pulse and decayed mostly as one component. All those observations are consistent with an accumulation of channels in O_1. A similar behavior was detected with ΔPASCap (Fig. 4B), albeit within a different voltage range, as could be predicted from the different voltage dependence of the transition between states (Fig. 2B). Again, alternating pulses resulted in larger current amplitudes and less complex tail current as compared to a single long pulse (Fig. 4B).

Deep-closed states favor access to O_1

A hallmark of $K_V10.1$ gating is the Cole-Moore shift, the change in activation kinetics in dependence on the pre-pulse potential (Cole and Moore, 1960). Hyperpolarized potentials drive the channel into deep closed states, which delays and decelerates activation (Ludwig et al., 1994;Hoshi and Armstrong, 2015). This is well described by a model with four identical, independent transitions of the voltage sensor (Schonherr et al., 1999) and is compromised by N-terminal deletions (Whicher and MacKinnon, 2019). To test the behavior of our mutants concerning this property, we applied a series of 5s-long conditioning pulses with voltages ranging from -160mV to -20mV, followed by a test pulse to +40mV in the absence of external

Cl^-. The activation kinetics, quantified by the time to 80% of the maximum current, showed a strong pre-pulse dependence in WT, ΔPASCap, and E600R, with much larger rise times in both mutants (Fig. 5B).

In the mutants, not only activation kinetics but also current amplitude was substantially affected by hyperpolarizing pre-pulses. With respect to the -100mV pre-pulse potential, the current starting from

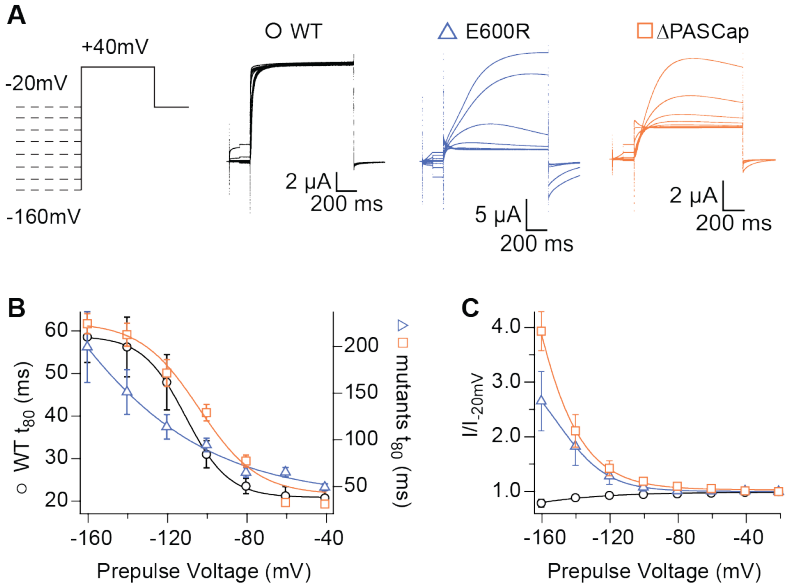

Figure 5. Hyperpolarization promotes access to a large conductance, slowly activating open state. A. Raw current traces in response to the stimuli depicted in the scheme. **B**. The rise time to 80% of the maximal current during the depolarizing stimulus is plotted *vs*. prepulse voltage (N: WT = 7, ΔPASCap = 9, E600R = 8; mean±SEM). Although the activation is much slower for both mutants (note the different y axis for the mutants), they retain a strong dependence on the prepulse potential. **C**. Normalized end-pulse current (I/I_{-20}) is plotted *vs*. prepulse voltage (N: WT = 10, ΔPASCap = 8, E600R = 8; mean±SEM). The amplitude of the current at +40 mV increased markedly when the holding potential was below -100 mV in the mutants, while the amplitude in WT changed only marginally.

a -160mV pre-pulse increased in ΔPASCap by a factor of 3.93 ± 0.36 and in E600R by a factor of 2.65 ± 0.54. In contrast, WT current amplitude was not significantly affected (Fig. 5A, 5C). Such increases in amplitude are often related to augmented channel availability due to voltage-dependent de-inactivation. Still, conventional inactivation was never detected in any mutants after repeated or prolonged depolarization. In the absence of inactivation, the prepulse-dependent current increase at +40 mV could be related to changes in the relative occupancy of the open states. We hypothesized that the higher conductance open state O_1 might be more accessible after hyperpolarization. The current decay after the peak (Fig. 5A), especially in ΔPASCap, also indicates a transient phenomenon. To map the voltage dependence of this effect more comprehensively, we next compared the effect of hyperpolarized pre-pulse on currents elicited at different test potentials.

We tested the effect of pre-pulse potentials (-160 and -100 mV) on IV protocols in the absence of Cl^-. Compared to a -100mV pre-pulse, -160mV clearly potentiated the first component of ΔPASCap and E600R biphasic IV (Fig. 6A and 6B).

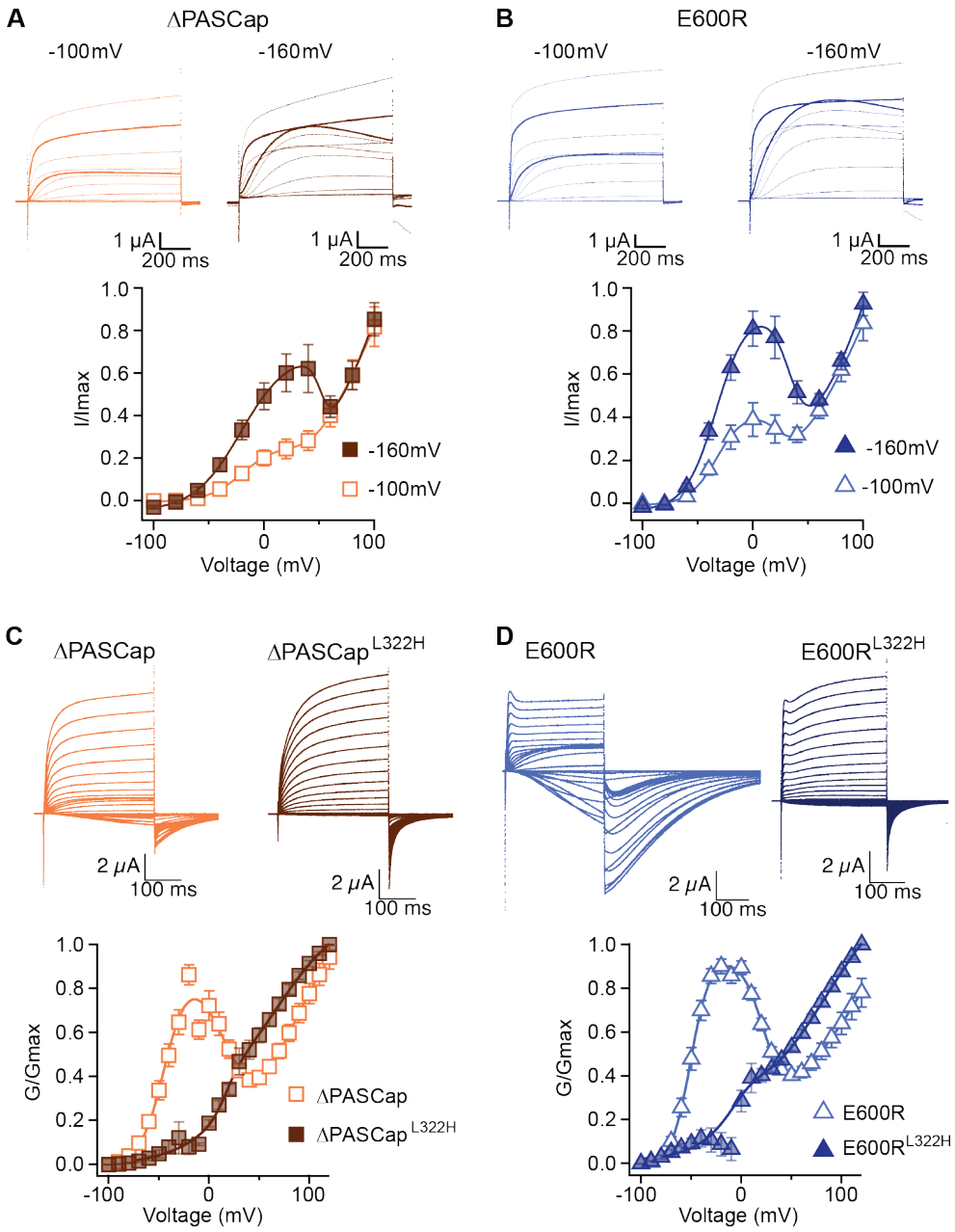

Figure 6. Deep closed states facilitate access to O_1. A, B. Conditioning pulses to -160 mV potentiated the first component and hence the biphasic behavior of the I/V relationships for ΔPASCap (A) and E600R (B). (N: ΔPASCap = 7, E600R = 6; mean±SEM) **C, D**. A mutation known to impair access to deep closed states (L322H) largely removes the initial phase of the GV curves for ΔPASCap (C) and E600R (D). (N: ΔPASCap = 7, $\Delta PASCap^{L322H}$ = 6, E600R = 11, $E600R^{L322H}$= 7; mean±SEM).

If the hyperpolarizing potentials facilitate the access to O_1 by driving the channel into deep closed states, then impairing the access to these states will reduce the component corresponding to O_1 in the GV. The mutation L322H, located in the S3-S4 linker, limits access to deep closed states in WT channels (Schonherr et al., 1999). We introduced this mutation in the context of ΔPASCap and E600R. Representative current traces obtained from $\Delta PASCap^{L322H}$ and $E600R^{L322H}$ are shown in Fig. 6 C and D. Both mutants showed drastic attenuation in the first component of the biphasic GV compared to the parental channels. The tail currents of $\Delta PASCap^{L322H}$ and $E600R^{L322H}$ did not show rectification. They presented homogenous kinetics at all potentials, indicating that reducing the access to deep closed states also reduces the occupancy of O_1.

Ca^{2+} Calmodulin stabilizes O_1

The available Cryo-EM structure shows $K_V10.1$ in a complex with Ca^{2+}-CaM. It is well established that the binding of a single Ca^{2+}-CaM inhibits the current through WT channels (Schonherr et al., 2000;Ziechner et al., 2006). In stark contrast, increasing intracellular Ca^{2+} has been reported to potentiate ΔPASCap and E600R current amplitudes (Lörinczi et al., 2016). This seemingly paradoxical behavior of mutants could be explained by the differential effects of Ca^{2+}-CaM binding on the availability of the two open states. The observations in WT and mutants would be consistent, with Ca^{2+} binding restricting access to the WT-like open state O_2 while facilitating access to the higher conductance state O_1 which is not visible in WT channels. Therefore, we predicted that Ca^{2+}-CaM would potentiate the first component of the biphasic IV in the mutants.

To test this, we induced a rise in cytosolic Ca^{2+} using the ionophore ionomycin and inducing release from the stores with thapsigargin (both 5µM) (Lörinczi et al., 2016). Because changes in intracellular Ca^{2+} are very dynamic (see Supp. 1 to Fig. 7) and our protocols with discrete voltage pulses require a long time to complete, we used a 5s voltage ramp from -120 to +100mV repeated every 30s for 300s. The currents were recorded in Cl^--free extracellular solution to avoid confounding effects of the endogenous Ca^{2+}-dependent Cl^- channels. The results of representative experiments on ΔPASCap and E600R are shown in the upper left panels of Fig. 7A and B, respectively. 60s after ionomycin/thapsigargin application, a marked

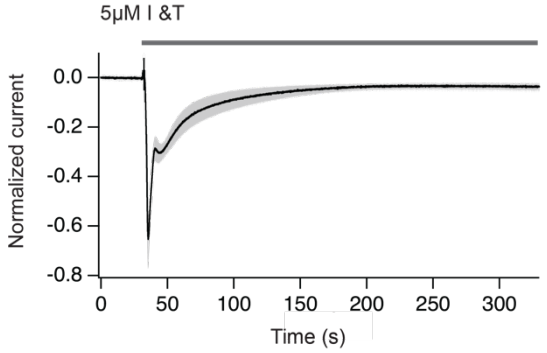

Supplement 1 to Figure 7. Chloride currents obtained upon treatment with ionomycin plus thapsigargin. The increase in cytosolic Ca^{2+} translates in a Cl^- current that can be used to estimate the amplitude and duration of the Ca^{2+} increase. Notice that Ca^{2+} returns to basal levels in approximately 150 s. The gray area indicates SEM. N=9

potentiation of the current amplitude was observed, and the response to the ramp became linear. The current amplitude declined over the following 300s, and the biphasic IV characteristics partly recovered. The speed and extent of recovery were higher for ΔPASCap than E600R; after 150s, 39.84± 6.35% recovery for ΔPASCap, while 11.84±3.07% recovered for E600R. This recovery time course agrees with the results obtained by Lörinzi et al. for constant pulses (Lörinczi et al., 2016). The magnitude of potentiation and change in IV shape was homogeneous enough among oocytes to allow averaging of the normalized current in all experiments (Fig. 7A and B, lower panel). The changes in slope can be easily observed in the corresponding first derivative of the normalized IV as a function of voltage shown in Supp. 2 to Fig. 7.

The changes in amplitude and kinetics in response to rising intracellular Ca^{2+} support our hypothesis that Ca^{2+}-CaM stabilizes O_1, possibly by driving the channels to deep closed states (Figs. 5 and 6). We, therefore, predicted that forcing the channels to deep closed states using Ca^{2+}-CaM could restore access to O_1 in $\Delta PASCap^{L322H}$ and $E600R^{L322H}$. This was tested with the approach described above, increasing intracellular Ca^{2+} while recording a repeated ramp protocol in $\Delta PASCap^{L322H}$ and $E600R^{L322H}$. As seen in the representative traces in the upper right panels in Fig. 7A and B, we observed a notable increase in current 60 s after Ca^{2+} rise, limited to *moderate* potentials, and resembling the first phase of the ramps in the parental mutants. For both mutants, the IV returned to a linear shape after 300s. Consistent with the observations for ΔPASCap and E600R, $\Delta PASCap^{L322H}$ exhibited faster recovery than $E600R^{L322H}$. Traces normalized to the maximum current and averaged are shown in Fig. 7A and B (lower panel). The respective first derivatives are shown in Supp. 3 to Fig. 7.

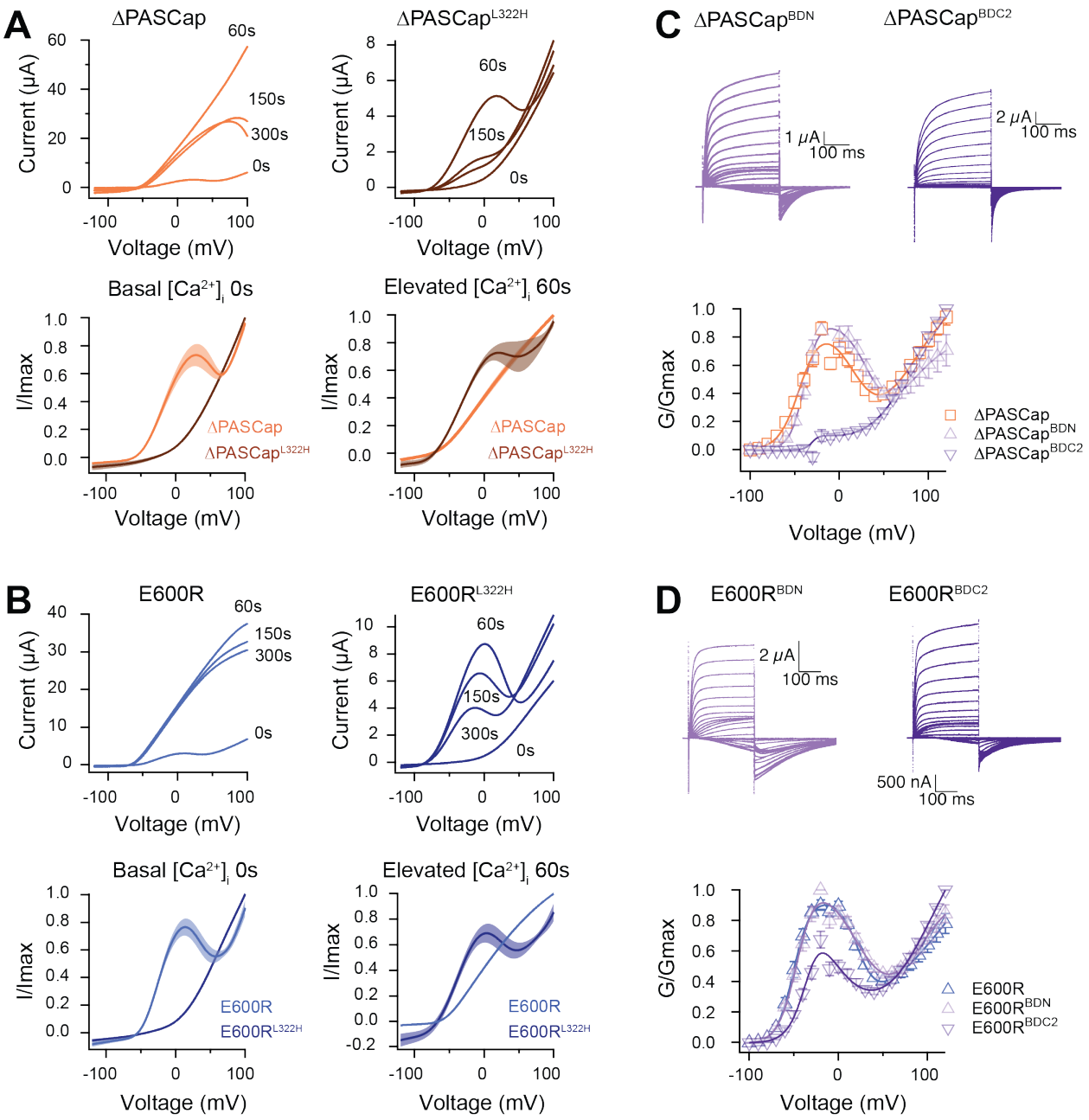

Figure 7. CaM stabilizes O_1. A. A transient rise in intracellular Ca^{2+} increases ΔPASCap current amplitude (in the absence of external chloride) and the IV relationship becomes linear (upper left traces). The lower traces represent the average normalized response comparing 0 and 60s. (ΔPASCap, light trace, N = 8, $\Delta PASCap^{L322H}$, dark trace, N= 5; the shadowed area indicates SEM). Right side traces: The same treatment in a channel carrying a mutation (L322H) reducing access to deep closed states results in the appearance of a biphasic IV upon Ca^{2+} rise. **B**. E600R behavior is comparable to ΔPASCap. Average normalized traces (E600R, light trace, N = 10; $E600R^{L322H}$, dark trace, N = 11; the shadowed area indicates SEM) are represented in the lower panel. **C**. Mutation of the C-terminal CaM binding domain (BDC2) in ΔPASCap reduces strongly the first component of the biphasic GV, while deletion of the N-terminal binding site (BDN) did not have any effect (N: ΔPASCap = 7, $\Delta PASCap^{BDN}$ = 7, $\Delta PASCap^{BDC2}$ = 7; mean ± SEM). **D**. The reduction of the first component in E600R when the C-terminal CaM binding site is mutated is also present but less intense. (N: E600R = 11, $E600R^{BDN}$ = 9, $E600R^{BDC2}$ = 11; mean±SEM)

To further explore the role of CaM, we introduced mutations to preclude CaM binding at the N-terminal

(F151N L154N) and C-terminal (F714S F717S) binding sites. We tested the behavior of these mutants (termed BDN and BDC2) in the context of ΔPASCap and E600R constructs (Fig 7C and D) under conditions of basal intracellular Ca^{2+} concentration. $\Delta PASCap^{BDN}$ showed a GV relationship like ΔPASCap. In contrast, $\Delta PASCap^{BDC2}$ lost its biphasic behavior. In the case of E600R, mutation of the C-terminal binding site ($E600R^{BDC2}$) showed attenuation of the first component of the GV, although not complete. The attenuation of the first component when binding of CaM is disrupted supports our hypothesis that Ca^{2+}CaM stabilizes O_1. The significance of CaM for the mutants seems different. CaM might be crucial for stabilizing O_1 in ΔPASCap, while less critical in E600R.

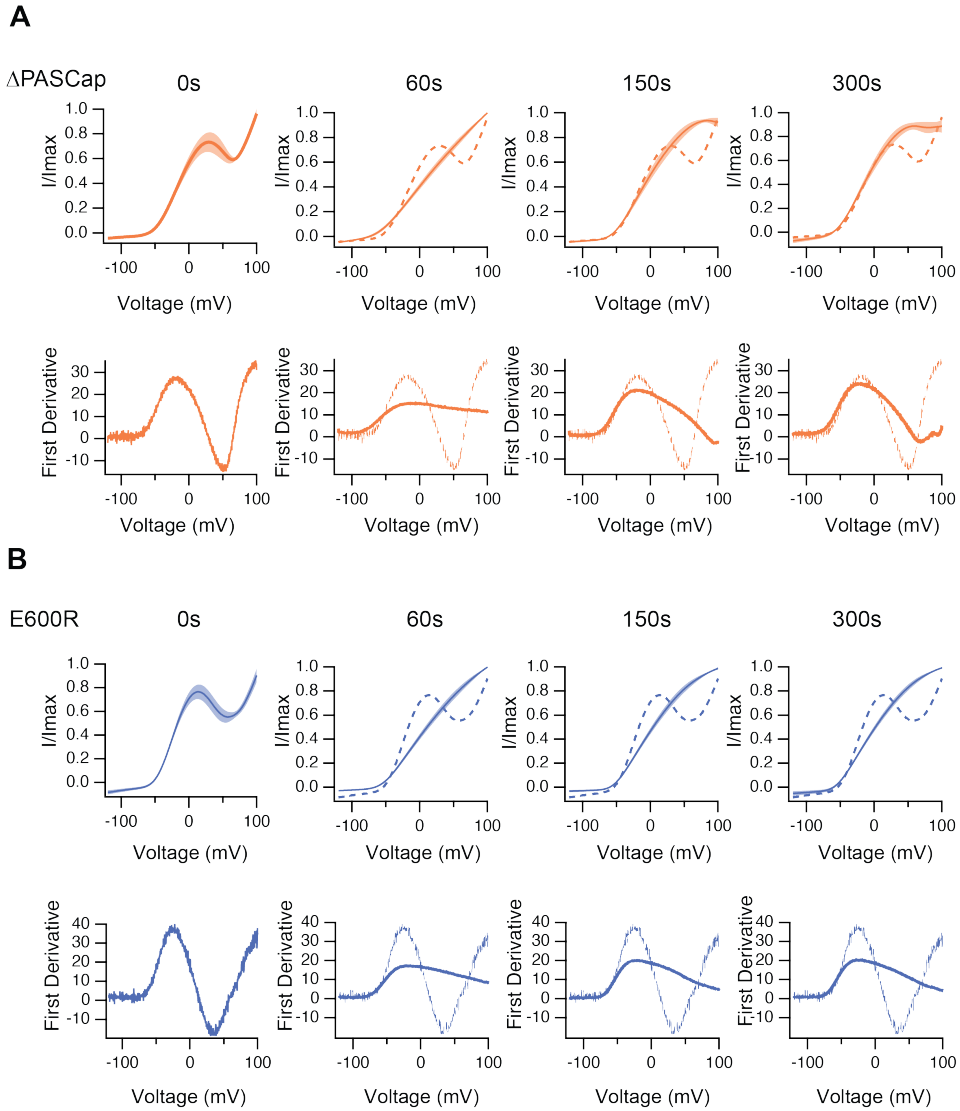

Supplement 2 to Figure 7. The upper traces show the average of normalized ramps at the indicated times for ΔPASCap (**A**) and E600R (**B**) after induction of Ca^{2+} rise. At 60, 150 and 300 s, the dashed line corresponds to the ramp at time 0. The shadowed area indicates SEM (N: ΔPASCap = 8, E600R = 10). The lower panels correspond to the first derivative of the current traces to illustrate the changes in slope.

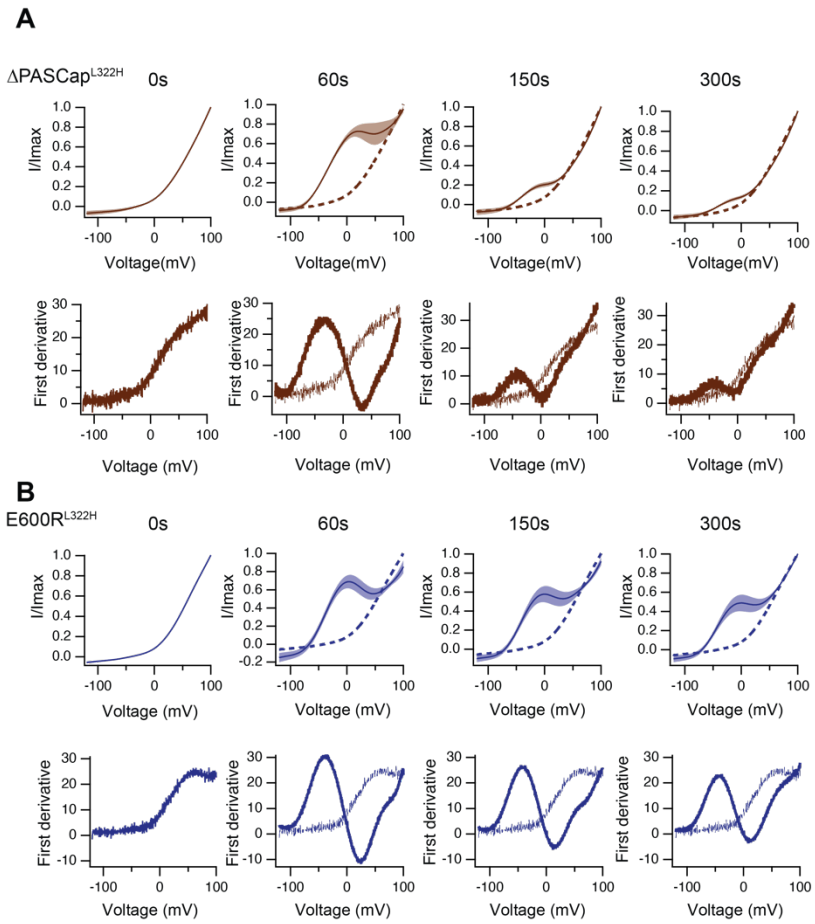

Supplement 3 to Figure 7. Like in Supplement 2, the upper traces show the average of normalized ramps for ΔPASCap^{L322H} (**A**) and E600^{L322H} (**B**) at the indicated times after induction of Ca^{2+} rise. At 60, 150 and 300 s, the dashed line corresponds to the ramp at time 0. The shadowed area indicates SEM (N: ΔPASCap^{L322H} = 5, E600R^{L322H} = 11). The lower panels correspond to the first derivative of the current traces to illustrate the changes in slope.

These results opened the possibility that the biphasic behavior is due to two coexisting populations of channels, depending on CaM binding at rest. We considered this possibility but we find it is unlikely, because: i) the behavior of the mutants is very homogeneous among oocytes, in which resting Ca^{2+} is very variable; it can be as high as 400 nM (Busa and Nuccitelli, 1985), although ten times lower concentrations have also been reported (Parker et al., 1996) and ii) two independent populations of channels would not explain the rectification or the voltage-dependent transitions during short repeated alternating stimuli.

Still, it was possible that CaM is permanently bound to the channel and participates in the gating machinery while only inhibiting the current when bound to Ca^{2+}. Although the available literature would not be compatible with this hypothesis (Schonherr et al., 2000;Ziechner et al., 2006), we estimated the fraction of channels (WT or mutant) bound to CaM as a function of free Ca^{2+} concentration. We co-expressed Myc-tagged CaM and K_V10.1, extracted the proteins in different Ca^{2+} concentrations (see Methods), and pulled

down the complex through the Myc-tag of CaM. Under these conditions, we could consistently detect a fraction of channels bound to CaM already in 50 and 100 nM Ca^{2+}, which increased dramatically in 0.5 and 1 μM, compatible with previous reports, suggesting that, at basal Ca^{2+}, only a small and variable fraction of channels are bound to CaM both in the WT and in the mutants (Supp. 4 to Fig. 7). The fraction of channels bound to CaM at basal Ca^{2+}, regardless of their stoichiometry (in the range of 4% in 100 nM, even if only one CaM is needed per channel tetramer), is insufficient to explain the prominent and proportionally constant first component observed in the mutants.

In summary, our results strongly suggest that Ca^{2+}-CaM stabilizes O_1, possibly by driving the channel to deep closed states.

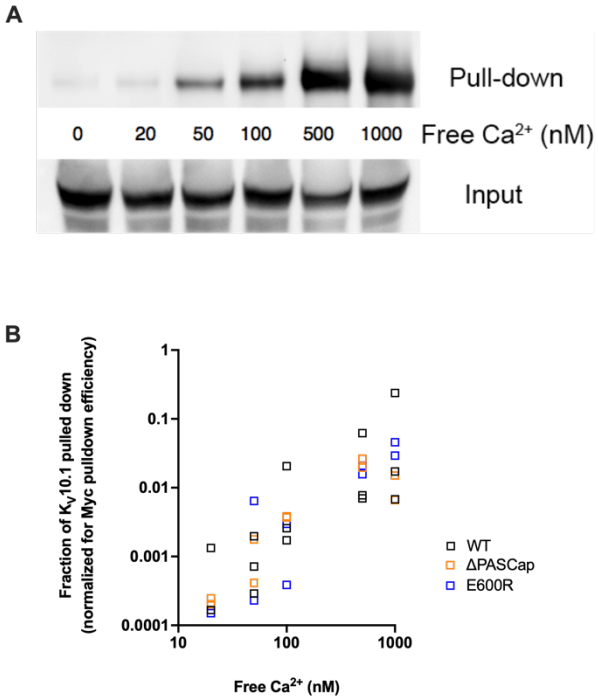

Supplement 4 to Figure 7. A. Ca^{2+}-dependent binding of CaM to $K_V10.1$. CaM was precipitated with anti-Myc antibody and the resulting pulled down fraction was immunoblotted using polyclonal anti- $K_V10.1$ antibody. **B** Quantification of all experiments reveals a strong dependence on Ca^{2+} concentration in WT and to a similar extent in mutant channels. The fraction of $K_V10.1$ pulled down increases by two orders of magnitude in high Ca^{2+}.

A two-layer Markov model recapitulates the kinetic features of ΔPASCap.

So far, our experimental results suggest that an additional open state exists in $K_V10.1$ mutants with a compromised intramolecular coupling. This hypothesis can explain the biphasic GV curves, the tail currents' complex shape (Fig. 1 and 2), the current increase following brief hyperpolarizations (Fig. 4), and even the paradoxical current increase under rising intracellular calcium concentrations (Fig. 7 and its supporting figures). However, in each case, there might be alternative explanations, such as two separate channel-populations with different properties, or voltage dependent de-inactivation. The ultimate test for the hypothesis is the construction of a single model that consistently and quantitatively captures all these unusual characteristics.

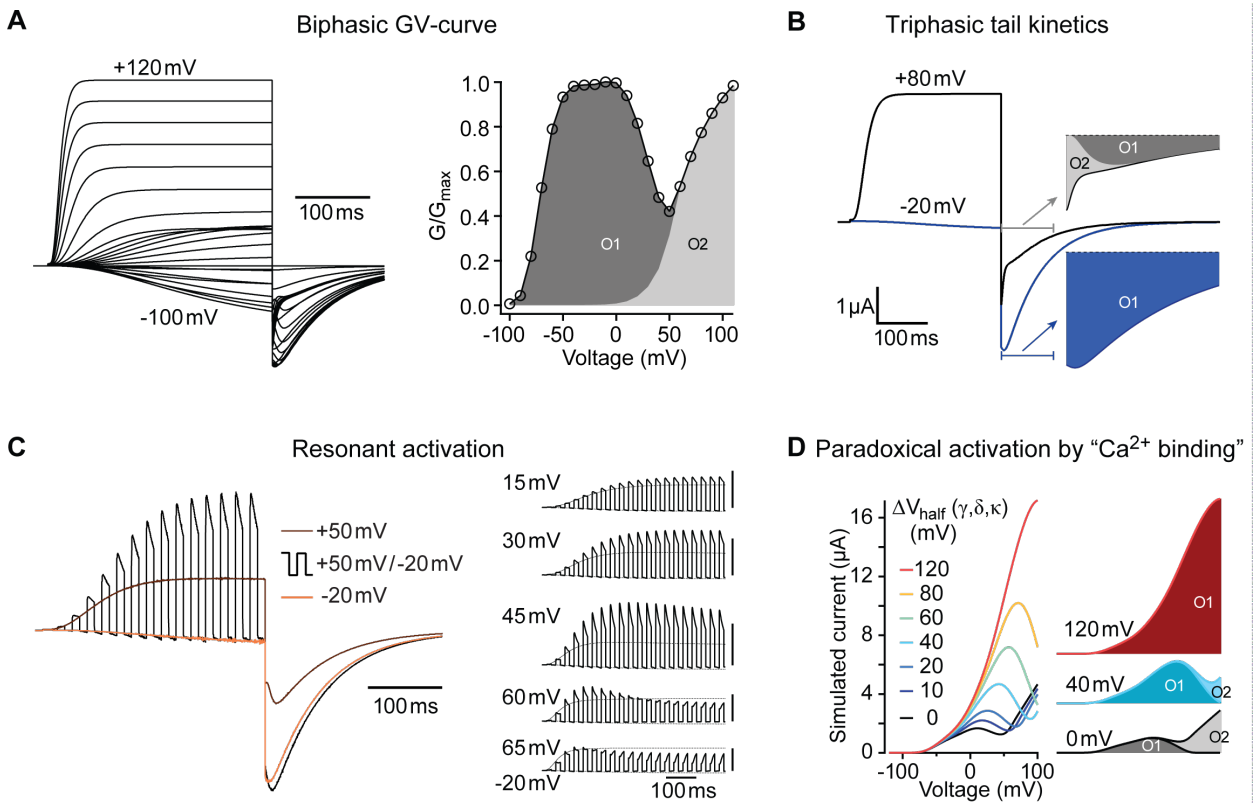

Figure 8. A single model can reproduce all experimental observations. A. In response to an I-V-protocol (Fig. 1A), the model displays biphasic activation, more clearly represented in the derived G-V curve (right, compare to Fig. 1B). The filled area indicates the contributions of the two open states. The tail-currents show a complex dependence on test-pulse voltage and time. **B**. Two traces from A, shown with longer repolarization. The first 100 ms of the tail currents are displayed on an extended timescale. The colored areas indicate the contributions of the two open states. After weak depolarization to -20mV, the tail-currents originate almost entirely from the mutant-specific open state O_1 (blue area). After strong depolarization, O_2 mediated currents initially dominate (light grey). The early, rapid decrease in current amplitude results from closure of O_2. During a delay phase, increasing current through an increasingly populated O_1 compensate for this closure, until eventually O_1 (dark grey) also closes, but with a much slower kinetics. **C**. In response to 10 ms pulses alternating between -20 and +50 mV, the model shows currents that exceed the currents obtained with constant pulses to +50 mV (compare Fig. 4 B). Relating the currents during the positive and negative pulses to the concurrent currents elicited by the two constant pulses (brown and orange), the ratio lies by about 1.6 for the period starting 200 ms after the pulse onset. This excess current depends sensitively on the duration and voltage of the two pulse components. The right series of simulations displays the results for 15 ms pulses to -20 mV, alternating with 15 ms pulses to voltages from 15mV to 65 mV. The corresponding responses to the constant pulses are displayed with thin dotted lines. To facilitate perception of the excess current, the five groups of traces are scaled individually, so that the peak amplitude of the dotted response elicited by the stronger depolarizations is displayed at equal size throughout. The vertical scalebars correspond to the same absolute current. From top to bottom, the excess current ratios at 200 ms changes are 1.05, 1.38, 1.74, 1.46, and 1.16. **D**. The binding of Ca^{2+}-CaM is implemented through change in the activation energy, corresponding to a shift in the equilibrium voltage of the gating transitions. The decomposition of the current into the individual open states' contribution shows that for increasing voltage shifts – representing high $[Ca^{2+}]_i$ – the mutant-specific O_1 closes later into the ramp, until eventually all current is carried by O_1.

We first tested whether simple addition of a second open state to the standard model of $K_V10.1$ activation (Schonherr et al., 1999), could replicate the experiments. However, none of these simple models could reproduce the pre-pulse dependence of entering O_1. Next, we introduced not only an additional open state, but also an additional gating step that is orthogonal to the standard model's transitions and might be related to a transition of the gating ring. This model successfully captured all the experimental observations (Figure 8 and supporting figures).

The standard model for $K_V10.1$ gating comprises two gating steps for each of the four subunits' voltage sensors. The first step unfolds in the hyperpolarized voltage range and forms the basis of the Cole-Moore shift, which is characteristic for $K_V10.1$ channel gating. The second, faster step readies the channel for opening, and once it is performed in all subunits, a conducting state can be reached (see also (Mandala and MacKinnon, 2022)). While this model captures the key features of WT activation, we had to extend it to account for the features of mutant gating. Throughout the model development and tuning, we focused on the experiments performed with the ΔPASCap mutant. However, a limited number of tests with other parameters showed that experimental findings with E600R can also be matched.

In a first step, we attempted a minimal model extension by attaching an additional open state to some closed state of the standard model. None of the resulting models could replicate all findings. Such a model could not replicate the multi-phasic tail currents, the pre-pulse dependence and the delayed opening under any choice of attachment site and rate voltage dependence. We came to this conclusion in two steps. First, we could exclude many possible attachment sites because the attachment site must be sufficiently far away from the conventional open state. Otherwise, the transition from "O_1 preferred" to "O_2 preferred" is very gradual and never produces the biphasic GV curves. Second, we found that the first gating transition in the standard model (left to right) can either produce a sigmoidal current onset or bias the model for occupancy of state O_1 over O_2. However, in the latter case, opening occurs without sigmoidal onset. Waveforms such as the dark orange trace in figure 5 A, in response to a -160 mV pre-pulse and a 20mV test pulse require both: a bias towards O_1 and a sigmoidal onset. We found that this can only be accounted for by introducing a third gating step, which is orthogonal to the two transitions in the standard model. Without *a priori* information about the new states introduced in this way, we decided to simply add a copy of the standard model as an additional layer, an "upper floor". Crossing from ground floor to upper floor was made possible for any state. From a structural view, this newly added transition might be related to a reconfiguration of the gating ring. Considerations as given above lead us to attach the mutant-specific O_1 to the basal level, and the conventional O_2 to the upper level. To explain the experiments, O_1 had to be accessible to states on the right of the ground floor, and not too far towards the bottom. Eventually, we decided to attach O_1 only to the state that corresponds to completion of the first gating step in all for subunits, but no other gating

step, neither the second voltage-sensor transition, nor the gating ring transition. In contrast, to enter O_2, all subunits must complete both voltage sensor transitions and also the collective gating ring transition.

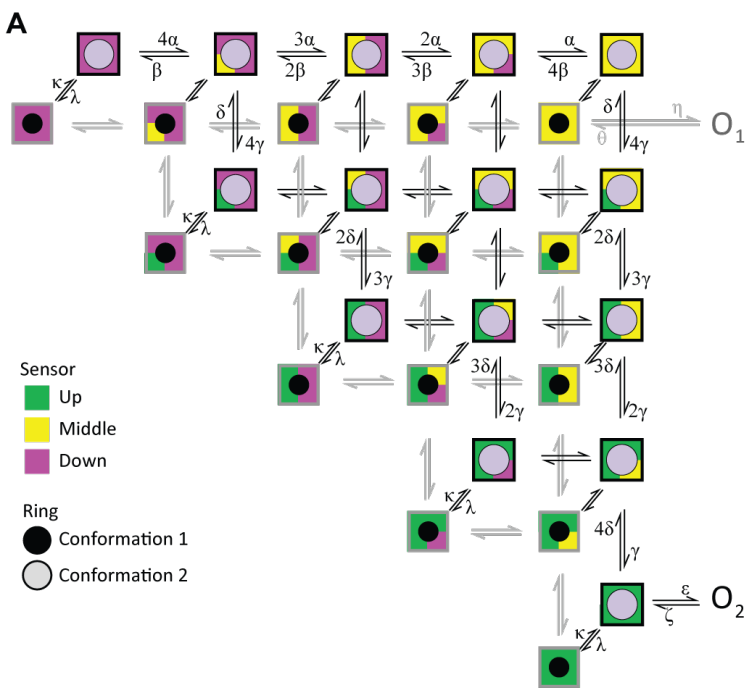

Supplement 1 to Figure 8. Cartoon depicting the state model proposed. A two-layer Markov-Model depicting possible conformations for the sensor and the ring. The sensor in each subunit can independently adopt one of three conformations (up, middle, and down) (Han et al., 2023). The up conformation represents the active conformation. The conformation of the ring changes across the two layers. The second conformation in the upper layer allows the channel to access "O_2" provided that all sensors are in the up conformation. Transitions within each layer is governed by (α, β, γ, δ), we proposed that the transitions are identical in the two layers. Transitions between the two levels are governed by the rate constants κ and λ

It should be noted that the model structure presented here is not the only one we found to be able to reproduce the data, but it is amongst the simplest that could. We also tested models in which the upper floor was only accessible from a subset of states, and models with O_1 attached to more than a single closed state or even multiple O_1 states with varying conductances. While those more complex models offered a gradual improvement matching experimental traces, they showed no striking advantages over the more symmetric and parsimonious model presented here.

We have extensively tested variants with this symmetric structure, with a broken symmetry in the gating kinetics. In these models, the conventional gating steps (left – right, top – bottom) differed between the ground floor and the newly introduced top floor states, e.g. by introduction of factors to the α, β, γ, δ values. Under these conditions, local balance was achieved by corresponding inverse factors to the local κ and λ.

Given the large number of model parameters (41+absolute conductance), it might be surprising that the parameters can be constrained. However, the wide range of voltage protocols and the concurrent matching of depolarization and repolarization responses tightly constrains several rate ratios at different voltages and thereby ultimately all parameters. Because the model does never fit all experiments very well, a global fit proved extremely hard to balance and we decided to explore the parameter space manually, based on the time constants and rate ratios we could discern from the experiments.

The resulting model was implemented in Igor Pro. The states and transitions were defined as depicted in Fig. S8-1. For the voltage dependent transition rates, we chose a sigmoidal functional form (Eq.1).

$$x = x_0 + \frac{A_x}{1+\exp\left(\left(V_m - V_x^h\right)\cdot k_x\right)} \qquad \text{Eq. 1}$$

where x stands one of the rates α, β, γ, δ, that govern transitions in the first and second dimension of the model, which we attribute to two sequential steps of voltage sensor displacement. The rates η and θ of opening and closing of the mutant-specific open state O_1 also follow this functional form, as does the rate λ, governing the return from the upper layer. The rate κ of entering the upper layer is the sum of two components, $\kappa_{all} = \kappa_l + \kappa_r$, which again follow the same functional form. The opening and closing rates of the second open state O_2, ε and ζ, are constants.

The parameters used for the simulation are shown in Table S2. The model defined by the structure in figure Supp. 1 to Fig. 8 and the voltage dependent rates in table S2 jointly define the model that produces all results in Fig. 8 and its supplementary figures. The only modification is done to capture the effect of Ca^{2+}-CaM-binding. If the binding influences the interaction between the intracellular modules that stabilize different configurations of the gating ring, e.g. BDC2, CNBHD, BDC1, PASCap, then the free energy of these states will change upon Ca^{2+}-CaM binding. Consequently, the free energy difference between the states and thereby the apparent voltage sensitivity of the transitions will change too. Hence, we represented the effect of different degrees of Ca^{2+}-CaM binding as different voltage shifts in λ, κ_L, γ, as indicated in figure 8D and Supp. 4 to Fig. 8.

rate x	x_0	A_x [s^{-1}]	V_{hx} [V]	K_x [V^{-1}]
α	8	192	0.09	-55
β	4	596	-0.13	80
γ	5	595	0.05	-30
δ	15	235	0.055	30
ε	200	0	—	—
ζ	120	0	—	—
η	100	400	0	-80
θ	20	80	0	-50
κ_R	0.125	69.875	-0.1	200
κ_L	0.125	499.875	0.09	-130
λ	0.1	999.9	-0.12	170

Table S2: parameters describing the voltage dependence of the transitions between states in the Markov model of K_V10.1 PASCap, in conjunction with Eq. 1.

While the Markov model describes the time and voltage dependence of state occupancies, the experimental observable is current. From the model, current was obtained by application of the GHK flux equation (equation 5) for both open states. The ratio between the conductances of the two opens states was adjusted to match experiments, in particular the pre-pulse-dependent activation: g_{O1}/g_{O2}=6.5.

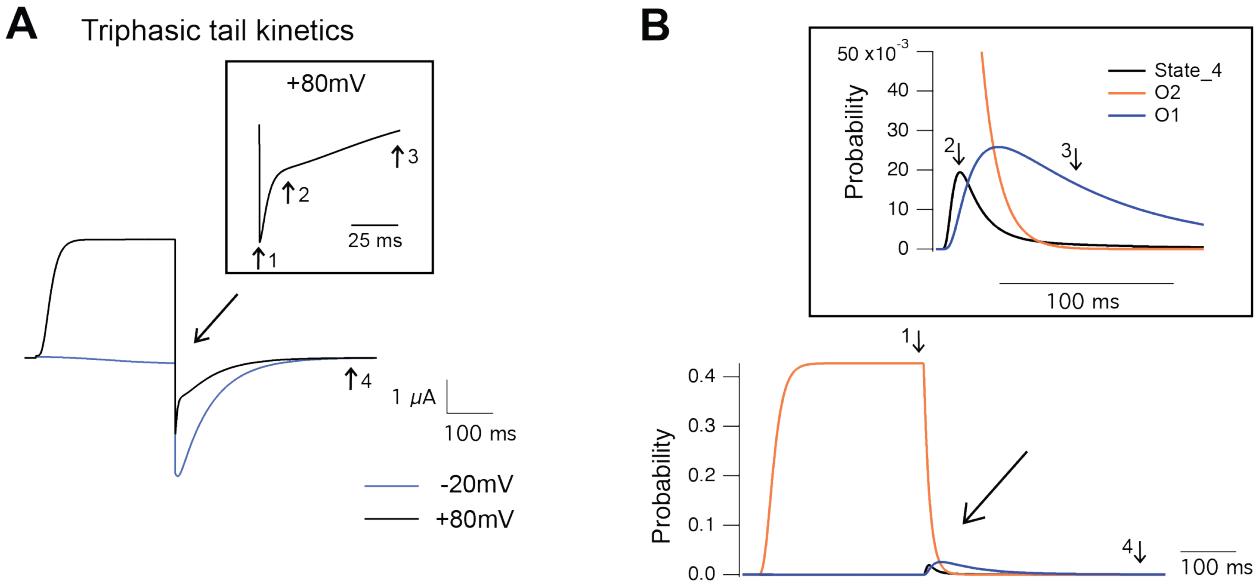

Supplement 2 to Figure 8. Current simulations for ΔPASCap upon depolarization to -20 or +80 mV in the presence of high extracellular K^+. **A**. The triphasic current kinetics (see Fig. 1E) observed experimentally at +80 mV (insert) is predicted by the model. **B**. Occupancy of State_4 (state closest to O_1), O_1 and O_2 as a function of time during a depolarization to +80 mV.

To test the model, we focused on the most conspicuous kinetics features observed with ΔPASCap. The first feature was the tail kinetics. In contrast to the slow monophasic deactivation observed in response to *weak* depolarizing pulses (-20mV), triphasic tail kinetics was detected in response to *strong* depolarizing pulses (+80mV) (Fig. 8B; Supp. 2 to Fig. 8). The model could replicate the slow deactivation after *weak* depolarizations, fast after *strong* depolarizations, and mixed kinetics on *moderate* stimuli.

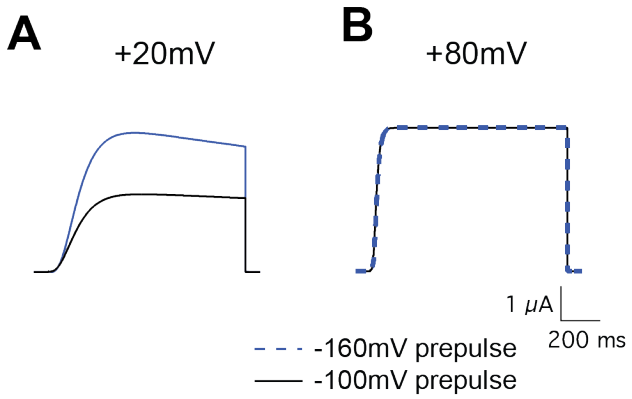

Supplement 3 to Figure 8. Current simulations for ΔPASCap upon depolarization to +20 and +80 mV after a conditioning pulse to -160 or -120 mV. The current at +20 mV is larger after -160 mV, while the current at +80 mV is unaffected by the conditioning pulse (see Fig. 6A)

The model also reproduces the effect of a hyperpolarizing pulse on different test potentials. As described (Fig. 6), O_1 is preferentially accessed from deep closed states, which correspond to states in the lower layer in the model. It is plausible that a hyperpolarizing pre-pulse (-160mV), drives the channel to occupy the deep closed states (lower layer), while a pre-pulse of –100mV distributes the channel between both layers. We, therefore, adjusted the parameters accordingly (Table S2) and simulated the current trace (Supp. 2 to Fig. 8) We focused on a test pulse that represents *moderate* depolarizations (+20mV), and compared it to a *strong* depolarizing pulse (+80mV). Like in the experiment, -160mV potentiates the current at +20mV, without impacting the current at +80mV (Supplement 2 to Fig. 8, A). This does not happen with -100mV pre-pulse (Supp. 2 to Fig. 8, B).

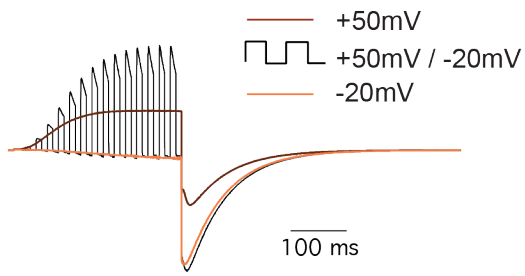

Supplement 4 to Figure 8. Current simulations for ΔPASCap upon alternating stimuli between -20 and +50 mV, as compared to sustained depolarization to each of the potentials (see Fig. 4B)

The model also recapitulates the behavior of ΔPASCap during repeated short stimuli between -20 and +50 mV. The amplitude of the intermittent stimuli is larger than that of a sustained stimulus to the same potential. It also reproduces the relative size and the kinetics of the tail current (Fig. 8C.; Supp. 4 to Fig. 8).

The effect of a rise in Ca^{2+} can be reproduced if the voltage dependence of the rate constants for transitions between the two layers are shifted to hyperpolarized potentials, increasing the probability of states in the "lower" layer and, therefore, of the access to O_1 (Fig. 8D; Supp. 5 to Fig. 8).

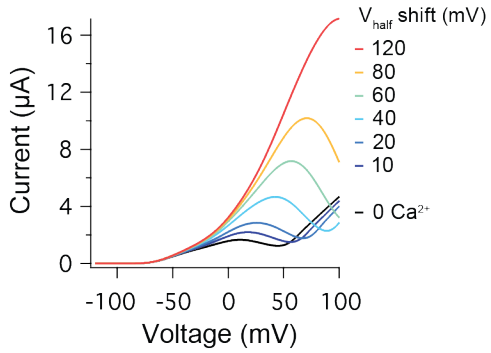

Supplement 5 to Figure 8. Current simulations for ΔPASCap under ramp depolarization using shifted rate constants (γ, δ, κ) to mimic the effect of CaM binding (see Fig. 7A)

To describe the behavior of $K_V10.1$ WT, we only needed to remove the access to O_1 and shift the parameters of the rotation of the ring in the hyperpolarizing direction to reflect the more stable structure resulting from intact interactions among intracellular domains and between these and the core of the channel. The model recapitulated the change in kinetics depending on the pre-pulse potential.

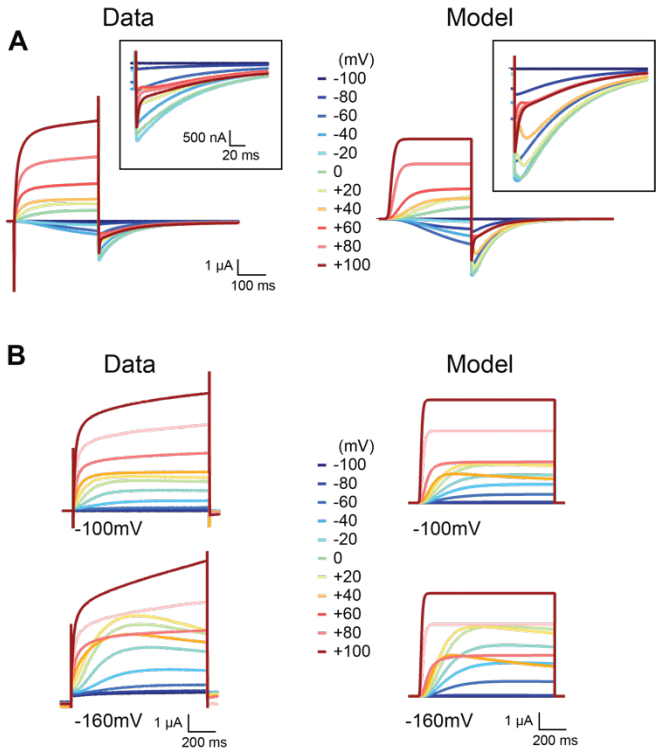

Supplement 6 to Figure 8. Side-by-side comparison of experimental data and model prediction during depolarizations between -100 and +100 mV in the presence of high (**A**) or low extracellular K^+ (**B**). the model describes the features of the current except the sustained rising phase during strong depolarizations.

Discussion

The wide diversity of electrical responses in cells relies greatly on subtle differences in the behavior of voltage-gated channels. Despite the many relevant advances in the knowledge of the structure of ion channels, the correlation between the structures and the functional determinants of channel behavior is incompletely understood. In this study, we have combined biophysical, biochemical, and mathematical approaches to understand the complex gating behavior of $K_V10.1$ potassium channels, which is the basis of a group of diseases with devastating consequences (e.g. (Toplak et al., 2022;Tian et al., 2023)).

In *KCNH* channels, intracellular domains contribute to gating by forming an intracellular ring that rotates in response to depolarizing stimuli (Mandala and MacKinnon, 2022). We have studied a series of mutant channels where the integrity of the intracellular ring is compromised by either deletions or point mutations. In all the mutants, the G-V relationship shows a biphasic behavior with evident inward rectification at intermediate depolarizations and a complex deactivation with kinetics also dependent on the stimulus potential (Fig. 1). Our observations can be explained by the coexistence of two different open states, one of which corresponds to the stable open state observed in WT (O_2), while the other one (O_1) is made visible as a result of the modification of the intracellular gating ring. We hypothesize that O_1 corresponds in the WT to the "non-conducting state 2" identified in the closely related $K_V10.2$ channel by cryo-EM (Tian et al., 2023), in which flipping of Y460 (Y464 in $K_V10.1$) renders a hydrophobic constriction wider than 8 Å, enough to allow K^+ flow, but still corresponds to a non-conducting state. The absence of an intact intracellular ring that would preclude ionic flow in the WT would explain the permeability of this state in the mutants.

Coexistence of two independent channel populations with different gating properties could be an alternative explanation for the observed behavior. Still, it is very unlikely that two such populations would be expressed at the same ratio in all oocytes, given the variability of the system, and the behavior of each of the mutants was highly reproducible among oocytes obtained from different frogs and time points.

The atypical open state O_1 allows the study of intermediate steps between the two major gating events, VSD displacement and ring rotation. Upon intermediate depolarization, the channels would access the open states sequentially, while O_2 is predominant on strong depolarizing steps and O_1 upon mild stimuli. The analysis of the GV of the mutants using global parameters (Fig. 2) revealed that they all share the component responding to mild depolarizations (O_1) and only the second component (O_2) and (probably most importantly) the transition between components depends on the particular mutant studied. The larger the deletion in the intracellular ring is, the stronger the shift in the voltage dependence of the second component. Importantly, this observation is incompatible with two independent populations of channels. Since the two gating steps are sequential (Mandala and MacKinnon, 2022), the displacement of the VSD remains the

main factor governing the speed and voltage dependence of the activation. Thus, changes in the extracellular Mg^{2+} concentration, which are known to interfere with the movement of the VSD (Silverman et al., 2004;Bannister et al., 2005), cause a shift of the voltage dependence and activation speed that affects both gating components (Fig. 3), but not the transition between them.

The biphasic behavior arises from a different conductance between the two open states, larger for O_1, that results in a decrease in current amplitude as the channels leave O_1 and transition to O_2. Since the time required to access the two states is different, when short alternating stimuli are applied, each with a too short duration to allow entry into O_2, the different conductance results in a larger current amplitude than when a single sustained stimulus is used (Fig. 4). The presence of a second state with larger conductance when the integrity of the ring is compromised could explain the larger current amplitudes observed in heteromeric $K_V11.1$ (HERG1a/1b) channels, which lack at least one PAS domain as a result of alternative splicing and are crucial for proper cardiac repolarization (Feng et al., 2021). Thus, the second open state could also have physiological relevance in naturally occurring channel complexes.

Access to O_1 is favored from deep deactivated states, which appear important in other aspects of $K_V10.1$ channel function (e.g., Cole-Moore shift). Our conclusion is based on the changes in amplitude observed with different pre-pulse potentials (that is, driving the population to deep closed states, Fig. 6A and B) and on the behavior of a mutant known to hinder access to such deactivated states (L322H), which, when combined with mutations revealing O_1, shows limited access to this state (Fig. 6C and D).

Ca^{2+}-CaM is an important modulator of $K_V10.1$ that reduces WT current amplitude in the presence of elevated Ca^{2+} levels. A paradoxical current increase had been described for some of the mutants used in this study (Lörinczi et al., 2016), and we speculated that the presence of O_1 could be the basis for this phenomenon. Indeed, the elevation of intracellular Ca^{2+} leads to a transient loss of the biphasic behavior and larger current amplitude of the mutants compatible with a larger fraction of channels in O_1. Because access to O_1 occurs from deep closed states, this could be explained by an increased occupancy of such deactivated states in response to CaM binding. This appears to be the case since CaM induces a biphasic behavior in the mutant channels that show reduced access to deep closed states; thus, L322H mutants behave like the parental variants in the presence of Ca^{2+}-CaM. This implies a mechanistic explanation for the effect of Ca^{2+}-CaM on WT since favoring entry into deep closed states would result in a decrease in current amplitude in the absence of (a permeable) O_1.

Our initial hypothesis that CaM participates constitutively in the gating machinery of the channel, based on the loss of biphasic behavior when the C-terminal binding site for CaM was mutated (Fig. 7D), is unlikely to be correct because although there is a significant binding of CaM to the channel at basal intracellular Ca^{2+}, this fraction of channels, combined with the strong increase in bound CaM in the presence of high

Ca^{2+} and the variable intracellular basal Ca^{2+} in oocytes would be insufficient to explain the qualitatively consistent behavior of the current of the different mutants. We speculate that the effects of the mutations in CaM binding sites are more related to their location in the protein than to their ability to bind CaM.

In summary, the gating of $K_V10.1$ (and similar channels) consists of a sequence of events that affect the voltage sensing domain, which moves in two sequential steps (Schonherr et al., 1999) and whose movement is transferred to the pore domain through intramolecular interactions (Bassetto et al., 2023). The voltage sensor maintains the gate closed (Mandala and MacKinnon, 2022), and its displacement has a permissive effect on gate opening. Once this restrictive factor is removed, a second step, most likely corresponding to a rotation of the intracellular ring, occurs and finally allows the gate to relax to the open state (Patlak, 1999). This final step is the only one directly observed in WT channels.

The presence of O_1 allowed us to model the behavior of the mutant channels based on a sequential "standard" Markovian model (Fig. 8 and its supplements). To recapitulate the experimental data, our model proposes two levels of deactivated states, one corresponding structurally to the displacement of the VSD, and one to the conformation of the intracellular ring. O_1 would be accessible when the movement of the VSD is partially completed, and O_2 would require both events to occur. The model recapitulates the biphasic activation in the I-V and G-V curves. It also accounts also for the complex dependence of test-pulse voltage and time in tail currents. After weak depolarization, the tail-currents originate almost entirely from the mutant-specific open state O_1, while after strong depolarization, O_2-mediated currents dominate in the beginning, while at later times an increasingly populated O_1 overcomes the fast deactivation of channels in O_2. O_1 then deactivates with a much slower kinetics.

The model also predicts the behavior of mutant channels under short alternating stimuli between -20 and +50 mV. The current amplitude is larger under these conditions than during constant pulses to +50 mV. Furthermore, it also accounts for the increased current amplitude observed after hyperpolarizing conditioning pulses, that is, when accessing from deep closed states (Suppl 3 to Fig.8). The binding of Ca^{2+}-CaM is implemented in the model through change in the activation energy, corresponding to a shift in the equilibrium voltage of the gating transitions. The decomposition of the current into the individual open states' contribution shows that for increasing voltage shifts – representing high $[Ca^{2+}]_i$ – the mutant-specific O_1 closes later into the ramp, until eventually all current is carried by O_1.

Still, our model does not account for certain kinetic features of the channel, most evidently the continued increase in current amplitude when the model predicts that steady-state should be achieved (Supp. 6 to Fig. 8).

In summary, this study presents a more complete description of the gating mechanism of $K_V10.1$ channel, which can be extended to other members of the *KCNH* family. In response to depolarization, the movement of the voltage sensor would have a permissive role for the opening of the gate. The rotation of the intracellular ring would be the effective unlocking mechanism allowing permeation. This has profound implication pertaining the possibilities of fine tuning of gating, since the intracellular ring is more susceptible of posttranslational modifications and protein-protein interactions than the transmembrane domains. Our current knowledge of the physiology and pathophysiology of $K_V10.1$ indicate that the channel is relevant for the regulation of excitability acting at potentials close to the resting, rather than during active electrical signaling. Therefore, sustained modulation of gating, possible through modification of the intracellular ring, would be crucial for channel function. Since they allow dissection of the ring-dependent effect, our mutants will allow for a direct study of such modulation mechanisms,

Materials and Methods

Constructs

Mutants were generated using K_V10.1 (hEAG1) cloned in pSGEM (M. Hollmann, Bochum University) as a template (Jenke et al., 2003). The deletion mutants, Δ2-10 and ΔPASCap, were generated using In-Fusion HD Cloning kit (Clontech (TaKaRA)) following the supplier's instructions. For each construct we designed two primers, each of them with two regions: a 3' region that anneals to the template immediately up- or downstream of the sequence to be deleted, and a 5' that does not bind to the template but overlaps with the second primer (Table S3). The subsequent PCR amplification will then omit the sequence between the hybridization sites for the primers.

To generate the point mutations ($\Delta PASCap^{L322H}$, $\Delta PASCap^{BDN}$, $\Delta PASCap^{BDC2}$, $E600R^{L322H}$, $E600R^{BDN}$, $E600R^{BDC2}$), site-directed mutagenesis was performed using Quick Change II XL kit (Agilent Technologies) using the primers listed in Table S3. E600R.pLeics71 and Δeag.pLeics71 were a gift from Dr. John Mitcheson, University of Leicester.

The expression construct for 5-myc-calmodulin was obtained by restriction cloning of CALM1 from pKK233-hCaM, which was a gift from Emanuel Strehler (Addgene plasmid # 47598) (Rhyner et al., 1992) into a pSGEM construct with five consecutive repeats of the myc tag (Lörinczi et al., 2015) using NcoI and HindIII (New England Biolabs).

All plasmids were linearized with NheI, and cRNA was synthesized using mMESSAGE mMACHINE T7 Transcription kit (Invitrogen Ambion).

Deletion/Mutation	Template (s)	Primers
2-10	pSGEM.Kv10.1 pSGEM Kv10.1 L341Split	F attcgatatcaagcttatggtggcccctcaaaacacgtttct R cggtatcgataagcttcagctggctccaaaaatgtctctct
ΔPASCap 2-25	pSGEM Kv10.1	F gctgccgccaccatg aatgatactaattttgtgttggggaa R catggtggcggcagctcg
ΔCNBHD 525-697	psGEM Kv10.1.	F tccagaggcattgac aatgaggcccccctgatcttgc R gtcaatgcctctggacatggaccaa
L322H	pSGEM Kv10.1 ΔPASCap pSGEM Kv10.1 E600R	F gatgagggcatcagcagccatttcagctctctaaaagttgt R acaacttttagagagctgaaatggctgctgatgccctcatc
N-terminal CaM binding site (BDN) F151NL154N	pSGEM Kv10.1 Δ2-10 pSGEM Kv10.1 ΔPASCap	F151N ctcttgtcagccgagcattcttcccccagcctttac L154N tgcttgtcagtgctcttgtattccgagcattcttcccccag
C-terminal CaM binding site (BDC2) F714SF717S	pSGEM Kv10.1 Δ2-10 pSGEM Kv10.1 ΔPASCap	F714S gtcggaatctctggctgaggcgccggacag F717S ctgctgtcggcttctctggctgaggcgccgg

Table S3. Primers used for infusion cloning or site-directed mutagenesis. The sequences are listed 5'-3'. For mutagenesis primers, only the sense sequences are given. The reverse primers corresponded to the reverse-complement sequence.

Two-Electrode Voltage-Clamp Recordings

Oocyte preparation and injection were performed as described (Stuhmer, 1992). The amount of cRNA injected depended on the current amplitude obtained with each construct: 0.075 - 0.5ng/oocyte (WT and point mutation), 0.075-5ng/oocyte (deletion mutants), and 8-10ng/oocyte (split channels). Oocytes were maintained at 18 °C in ND96 buffer (in mM: 96 NaCl, 2 KCl, 1.8 $CaCl_2$, 1 $MgCl_2$, 5 HEPES, 2.5 Na-pyruvate, 0.5 Theophylline, pH 7.55). Tetracycline (USB) (50µg/ml), Amikacin (Enzo) (100µg/ml) and Ciprofloxacin (Enzo) (100µg/ml) were added as recommended in (O'Connell et al., 2011).

Two-electrode voltage-clamp (TEVC) recordings were performed 1-5 days after oocyte injection. The intracellular electrodes had a resistance of 0.4-1.5 MΩ when filled with 2M KCl. Normal Frog Ringer solution (NFR): (in mM: 115 NaCl, 2.5 KCl, 10 HEPES, 1.8 $CaCl_2$, pH 7.2), was used as external solution. Higher K^+ concentration (mM: 60 KCl, 57.5 NaCl, 10 HEPES, 1.8 $CaCl_2$, pH=7.4), was used instead to examine tail currents. Cl^- free NFR (in mM: 115 Na-methanesulfonate, 2.5 KOH, 10 HEPES, 1.8 $Ca(OH)_2$, pH=7.2), was used to limit current contamination with Cl^- current; in this case, agar bridges (2% agar in 3M NaCl) were used for the reference electrodes. To raise the intracellular Ca^{2+} concentration (Lörinczi et al., 2016), 5µM ionomycin (Abcam) and 5µM Thapsigargin (Abcam) were added to the bath. Ionomycin and Thapsigargin 5mM stocks was prepared using DMSO and diluted in the recording medium (Cl^- free NFR) immediately before recording. The final concentration of DMSO was thus 0.1%.

Data acquisition was performed using a TurboTEC 10-CD amplifier (npi Electronics) and the ITC-16 interface of an EPC9 patch-clamp amplifier (HEKA Elektronik). The current was filtered at 1.3 KHz and sampled at 10 KHz. Patchmaster software (HEKA Elektronik) was used to design and apply the stimulus protocols applied. Because of the profound effects of hyperpolarization on channel kinetics, leak subtraction was avoided except when explicitly indicated. Fitmaster (HEKA Elektronik) and IgorPro (WaveMetrics) were then used to analyze the recordings.

Most conductance-voltage plots are obtained for recordings with $[K^+]_{ext}$ =60mM. In this condition, tail currents are large and allow precise estimation of the reversal potential V_{eq}. Under this condition, the difference between intra- and extracellular potassium concentration is small and the Goldman-Hodgkin-Katz flux equation predicts a nearly linear relation. In these cases, conductance was calculated from the end-pulse current after measuring the reversal potential (V_{eq}) using:

$$G = I / (V_m - V_{eq})$$ Eq.2

where I is the current amplitude and V_m the stimulus. Conductance was then normalized to the maximum value and plotted against voltage stimulus. For WT recordings (Fig. 1B), a sigmoidal response was then fitted with a Boltzmann equation:

$$f(V) = \left(1 + \exp\left((V_h - V_m)/K\right)\right)^{-1}$$ Eq.3

With V_h being the voltage for half-maximal activation, K the slope factor and V_m the membrane potential as above.

The biphasic response we observed in the mutants was described with two sigmoidal components and a weight W to represent the transition between the two components. The equation used was as follows:

$$f(V) = A_o + \left(1 - \mathrm{W}(V)\right) \cdot \mathrm{A}_1 \cdot \left(1 + e^{(V_{h1} - V_m)/K_1}\right)^{-1} + \mathrm{W}(V) \cdot \mathrm{A}_2 \cdot \left(1 + e^{(V_{h2} - V_m)/K_2}\right)^{-1}$$

$$\mathrm{W}(V) = \left(1 + e^{(V_{h3} - V_m)/K_3}\right)^{-1}$$ Eq.4

If the currents were recorded in $[K^+]_{ext}$=2.5 mM, the driving force for currents becomes considerably non-linear (Kotler et al., 2022)and we estimated the conductance based on the full Goldman-Hodgkin-Katz flux equation for a current surface density Φ.

$\Phi = P \cdot P^{open} \cdot zF \cdot \frac{V_m}{V_T}\left(\frac{[K^+]_{in} - [K^+]_{out} \cdot e^{-V_m/V_T}}{1 - e^{-V_m/V_T}}\right)$, where $V_T = \frac{RT}{zF}$,with the gas constant *R,* the Faraday constant *F*, the absolute temperature *T*, the potassium channel open probability P^{open} , and the maximum permeability *P.* The ions valence *z* equals 1. Because we only work with normalized conductances, the following relation can be used to determine the voltage dependent conductance:

$$G(V) \propto I \cdot \left(\frac{1 - e^{-V_m/V_T}}{[K^+]_{in} - [K^+]_{out} e^{-V_m/V_T}}\right) \cdot \frac{V_T}{zFV_m}$$

Eq.5

Pull-down

Xenopus laevis oocytes were co-injected with RNA coding for 5xmyc-calmodulin (10ng) and $K_V10.1$ (0.5ng). Oocytes were lysed 72 h after injection through mechanical disruption in lysis buffer and incubation for 30 min on ice. The lysis buffer (1% Triton X-100, 150 mM NaCl, 50 mM HEPES pH 7.4, cOmplete EDTA-free protease inhibitor cocktail (Roche)) contained different free Ca^{2+} concentrations (0 nM, 20 nM, 50 nM, 100 nM, 500 nM, 1µM). To obtain accurate Ca^{2+} concentrations, EGTA was titrated

with $CaCal_2$, to prepare 100mM CaEGTA stock solution as described in (Tsien and Pozzan, 1989). CaEGTA and EGTA were then added to the lysis buffer, adjusting EGTA/CaEGTA to control the concentration of free Ca^{2+} taking into account pH, ionic strength and temperature of solution using MaxChelator (Bers et al., 2010) As controls, non-injected oocytes, and oocytes injected with only $K_V10.1$ or 5xmyc-calmodulin were lysed in a Ca^{2+} free buffer.

The lysate was then centrifuged (20,000 x*g*) at 4 °C for 3 min to remove debris. 10% of the supernatant was set aside to load on the gel as input control. The lysate was pre-cleared using protein G magnetic beads (New England Biolabs). The cleared supernatant was then incubated with 3 µg anti-myc antibody (SIGMA M4439 monoclonal anti c-myc or Abcam ab206486 rat mAb to myc tag (9E10)) for 1.5h at 4 °C. Protein G magnetic beads were then added and incubated for 1.5h at 4 °C in rotation. After magnetic retrieval, the beads were washed three times using 0.1% Triton X-100, 300 mM NaCl, 50 mM HEPES pH 7.4, cOmplete (EDTA-free protease inhibitor cocktail), EGTA and CaEGTA to obtain the corresponding Ca^{2+}-free concentrations (see above). Electrophoresis and immunoblotting conditions were as previously described (Lörinczi et al., 2015) using an anti-Myc (Sigma, 1:1000) or an anti- $K_V10.1$ antibody (Chen et al., 2011) overnight.

Acknowledgements.

We thank the expert technical assistance of Kerstin Dümke. RA was supported by an IMPRS Neurosciences scholarship.

Data availability

The authors declare that the data supporting the findings of this study are available within the paper and its supplementary information files.

REFERENCES

Babu, Y.S., Sack, J.S., Greenhough, T.J., Bugg, C.E., Means, A.R., and Cook, W.J. (1985). Three-dimensional structure of calmodulin. *Nature* 315**,** 37-40. doi: 10.1038/315037a0

Bannister, J.P., Chanda, B., Bezanilla, F., and Papazian, D.M. (2005). Optical detection of rate-determining ion-modulated conformational changes of the ether-a-go-go K+ channel voltage sensor. *Proc Natl Acad Sci U S A* 102**,** 18718-18723. doi:

Barros, F., De La Pena, P., Dominguez, P., Sierra, L.M., and Pardo, L.A. (2020). The EAG Voltage-Dependent K(+) Channel Subfamily: Similarities and Differences in Structural Organization and Gating. *Front Pharmacol* 11**,** 411. doi: 10.3389/fphar.2020.00411

Bassetto, C.a.Z., Jr., Costa, F., Guardiani, C., Bezanilla, F., and Giacomello, A. (2023). Noncanonical electromechanical coupling paths in cardiac hERG potassium channel. *Nat Commun* 14**,** 1110. doi: 10.1038/s41467-023-36730-7

Bauer, C.K., and Schwarz, J.R. (2018). Ether-à-go-go K+ channels: effective modulators of neuronal excitability. *The Journal of Physiology* 596**,** 769-783. doi: 10.1113/JP275477

Bers, D.M., Patton, C.W., and Nuccitelli, R. (2010). A Practical Guide to the Preparation of Ca2+ a Buffers. *Calcium in Living Cells* 99**,** 1-26. doi: 10.1016/S0091-679x(10)99001-8

Busa, W.B., and Nuccitelli, R. (1985). An elevated free cytosolic Ca2+ wave follows fertilization in eggs of the frog, Xenopus laevis. *J Cell Biol* 100**,** 1325-1329. doi: 10.1083/jcb.100.4.1325

Chen, Y., Sánchez, A., Rubio, M.E., Kohl, T., Pardo, L.A., and Stühmer, W. (2011). Functional Kv10.1 Channels Localize to the Inner Nuclear Membrane. *PLoS ONE* 6**,** e19257. doi: 10.1371/journal.pone.0019257

Codding, S.J., Johnson, A.A., and Trudeau, M.C. (2020). Gating and regulation of KCNH (ERG, EAG, and ELK) channels by intracellular domains. *Channels (Austin)* 14**,** 294-309. doi: 10.1080/19336950.2020.1816107

Codding, S.J., and Trudeau, M.C. (2019). The hERG potassium channel intrinsic ligand regulates N- and C-terminal interactions and channel closure. *J Gen Physiol* 151**,** 478-488. doi: 10.1085/jgp.201812129

Cole, K.S., and Moore, J.W. (1960). Potassium ion current in the squid giant axon: dynamic characteristic. *Biophys J* 1**,** 1-4. doi:

Dai, G., James, Z.M., and Zagotta, W.N. (2018). Dynamic rearrangement of the intrinsic ligand regulates KCNH potassium channels. *The Journal of General Physiology*. doi:

Dai, G., and Zagotta, W.N. (2017). Molecular mechanism of voltage-dependent potentiation of KCNH potassium channels. *eLife* 6**,** e26355. doi: 10.7554/eLife.26355

De La Pena, P., Dominguez, P., and Barros, F. (2018). Gating mechanism of Kv11.1 (hERG) K(+) channels without covalent connection between voltage sensor and pore domains. *Pflugers Arch* 470**,** 517-536. doi: 10.1007/s00424-017-2093-9

Feng, L., Zhang, J., Lee, C., Kim, G., Liu, F., Petersen, A.J., Lim, E., Anderson, C.L., Orland, K.M., Robertson, G.A., Eckhardt, L.L., January, C.T., and Kamp, T.J. (2021). Long QT Syndrome KCNH2 Variant Induces hERG1a/1b Subunit Imbalance in Patient-Specific Induced Pluripotent Stem Cell-Derived Cardiomyocytes. *Circ Arrhythm Electrophysiol* 14**,** e009343. doi: 10.1161/CIRCEP.120.009343

Gianulis, E.C., Liu, Q., and Trudeau, M.C. (2013). Direct interaction of eag domains and cyclic nucleotide–binding homology domains regulate deactivation gating in hERG channels. *The Journal of General Physiology* 142**,** 351-366. doi: 10.1085/jgp.201310995

Gonçalves, J.T., and Stühmer, W. (2010). Calmodulin Interaction with hEAG1 Visualized by FRET Microscopy. *PLoS ONE* 5**,** e10873. doi: 10.1371/journal.pone.0010873

Haitin, Y., Carlson, A.E., and Zagotta, W.N. (2013). The structural mechanism of KCNH-channel regulation by the eag domain. *Nature* 501**,** 444-448. doi: 10.1038/nature12487

http://www.nature.com/nature/journal/v501/n7467/abs/nature12487.html#supplementary-information

Han, S., Vance, J., Jones, S., Decata, J., Tran, K., Cummings, J., and Wang, S. (2023). Voltage sensor dynamics of a bacterial voltage-gated sodium channel NavAb reveal three conformational states. *J Biol Chem* 299**,** 102967. doi: 10.1016/j.jbc.2023.102967

Harley, C.A., Bernardo-Seisdedos, G., Stevens-Sostre, W.A., Jones, D.K., Azevedo, M.M., Sampaio, P., Lorga-Gomes, M., Trudeau, M.C., Millet, O., Robertson, G.A., and Morais-Cabral, J.H. (2021). Conformation-sensitive antibody reveals an altered cytosolic PAS/CNBh assembly during hERG channel gating. *Proc Natl Acad Sci U S A* 118. doi: 10.1073/pnas.2108796118

Hoshi, T., and Armstrong, C.M. (2015). The Cole-Moore Effect: Still Unexplained? *Biophys J* 109**,** 1312-1316. doi: 10.1016/j.bpj.2015.07.052

James, Z.M., and Zagotta, W.N. (2017). Structural insights into the mechanisms of CNBD channel function. *The Journal of General Physiology*. doi: 10.1085/jgp.201711898

Jenke, M., Sanchez, A., Monje, F., Stuhmer, W., Weseloh, R.M., and Pardo, L.A. (2003). C-terminal domains implicated in the functional surface expression of potassium channels. *EMBO J* 22**,** 395-403. doi: 10.1093/emboj/cdg035

Ju, M., and Wray, D. (2006). Molecular regions responsible for differences in activation between heag channels. *Biochem Biophys Res Commun* 342**,** 1088--1097. doi:

Kotler, O., Gutnick, M.J., and Fleidervish, I.A. (2022). In computational models, action potential propagation in ultrathin axons is resilient despite considerable intracellular Na(+) accumulation. *Proc Natl Acad Sci U S A* 119**,** e2120782119. doi: 10.1073/pnas.2120782119

Lörinczi, É., Gómez-Posada, J.C., De La Peña, P., Tomczak, A.P., Fernández-Trillo, J., Leipscher, U., Stühmer, W., Barros, F., and Pardo, L.A. (2015). Voltage-dependent gating of KCNH potassium channels lacking a covalent link between voltage-sensing and pore domains. *Nat Commun* 6**,** 6672. doi: 10.1038/ncomms7672

Lörinczi, E., Helliwell, M., Finch, A., Stansfeld, P.J., Davies, N.W., Mahaut-Smith, M., Muskett, F.W., and Mitcheson, J.S. (2016). Calmodulin Regulates Human Ether à Go-Go 1 (hEAG1) Potassium Channels through Interactions of the Eag Domain with the Cyclic Nucleotide Binding Homology Domain. *Journal of Biological Chemistry* 291**,** 17907-17918. doi: 10.1074/jbc.M116.733576

Ludwig, J., Terlau, H., Wunder, F., Bruggemann, A., Pardo, L.A., Marquardt, A., Stuhmer, W., and Pongs, O. (1994). Functional expression of a rat homologue of the voltage gated either a go-go potassium channel reveals differences in selectivity and activation kinetics between the Drosophila channel and its mammalian counterpart. *EMBO J* 13**,** 4451-4458. doi:

Malak, O.A., Gluhov, G.S., Grizel, A.V., Kudryashova, K.S., Sokolova, O.S., and Loussouarn, G. (2019). Voltage-dependent activation in EAG channels follows a ligand-receptor rather than a mechanical-lever mechanism. *J Biol Chem*. doi: 10.1074/jbc.RA119.007626

Mandala, V.S., and Mackinnon, R. (2022). Voltage-sensor movements in the Eag Kv channel under an applied electric field. *Proc Natl Acad Sci U S A* 119**,** e2214151119. doi: 10.1073/pnas.2214151119

Nunez, E., Muguruza-Montero, A., and Villarroel, A. (2020). Atomistic Insights of Calmodulin Gating of Complete Ion Channels. *Int J Mol Sci* 21. doi: 10.3390/ijms21041285

O'connell, D., Mruk, K., Rocheleau, J.M., and Kobertz, W.R. (2011). *Xenopus laevis* oocytes infected with multi-drug–resistant bacteria: implications for electrical recordings. *The Journal of General Physiology* 138**,** 271-277. doi: 10.1085/jgp.201110661

Parker, I., Choi, J., and Yao, Y. (1996). Elementary events of InsP3-induced Ca2+ liberation in Xenopus oocytes: hot spots, puffs and blips. *Cell Calcium* 20**,** 105-121. doi: 10.1016/s0143-4160(96)90100-1

Patlak, J.B. (1999). Cooperating to unlock the voltage-dependent K channel. *J Gen Physiol* 113**,** 385-388. doi: 10.1085/jgp.113.3.385

Rhyner, J.A., Koller, M., Durussel-Gerber, I., Cox, J.A., and Strehler, E.E. (1992). Characterization of the human calmodulin-like protein expressed in Escherichia coli. *Biochemistry* 31**,** 12826-12832. doi: 10.1021/bi00166a017

Sahoo, N., Schonherr, R., Hoshi, T., and Heinemann, S.H. (2012). Cysteines control the N- and C-linker-dependent gating of KCNH1 potassium channels. *Biochim Biophys Acta* 1818**,** 1187-1195. doi: 10.1016/j.bbamem.2012.01.021

Schonherr, R., Hehl, S., Terlau, H., Baumann, A., and Heinemann, S.H. (1999). Individual subunits contribute independently to slow gating of bovine EAG potassium channels. *Journal of Biological Chemistry* 274**,** 5362-5369. doi:

Schonherr, R., Lober, K., and Heinemann, S.H. (2000). Inhibition of human ether a go-go potassium channels by Ca(2+)/calmodulin. *Embo J* 19**,** 3263-3271. doi:

Silverman, W.R., Bannister, J.P.A., and Papazian, D.M. (2004). Binding Site in Eag Voltage Sensor Accommodates a Variety of Ions and is Accessible in Closed Channel. *Biophysical Journal* 87**,** 3110-3121. doi: 10.1529/biophysj.104.044602

Silverman, W.R., Tang, C.Y., Mock, A.F., Huh, K.B., and Papazian, D.M. (2000). Mg(2+) modulates voltage-dependent activation in ether-a-go-go potassium channels by binding between transmembrane segments S2 and S3. *Journal of General Physiology* 116**,** 663-678. doi: 10.1085/jgp.116.5.663

Stuhmer, W. (1992). Electrophysiological recording from Xenopus oocytes. *Methods Enzymol* 207**,** 319-339. doi:

Tang, C.-Y., Bezanilla, F., and Papazian, D.M. (2000). Extracellular Mg2+ Modulates Slow Gating Transitions and the Opening of Drosophila Ether-à-Go-Go Potassium Channels. *The Journal of General Physiology* 115**,** 319-338. doi: 10.1085/jgp.115.3.319

Terlau, H., Heinemann, S.H., Stuhmer, W., Pongs, O., and Ludwig, J. (1997). Amino terminal-dependent gating of the potassium channel rat eag is compensated by a mutation in the S4 segment. *Journal of Physiology* 502**,** 537-543. doi: 10.1111/j.1469-7793.1997.537bj.x

Terlau, H., Ludwig, J., Steffan, R., Pongs, O., Stühmer, W., and Heinemann, S. (1996). Extracellular Mg2+ regulates activation of rat eag potassium channel. *Pflügers Archiv European Journal of Physiology* 432**,** 301-312. doi: 10.1007/s004240050137

Thouta, S., Sokolov, S., Abe, Y., Clark, Sheldon j., Cheng, Yen m., and Claydon, Tom w. (2014). Proline Scan of the hERG Channel S6 Helix Reveals the Location of the Intracellular Pore Gate. *Biophysical Journal* 106**,** 1057-1069. doi: http://dx.doi.org/10.1016/j.bpj.2014.01.035

Tian, M.Q., Li, R.K., Yang, F., Shu, X.M., Li, J., Chen, J., Peng, L.Y., Yu, X.H., and Yang, C.J. (2023). Phenotypic expansion of KCNH1-associated disorders to include isolated epilepsy and its associations with genotypes and molecular sub-regional locations. *CNS Neurosci Ther* 29**,** 270-281. doi: 10.1111/cns.14001

Tomczak, A.P., Fernández-Trillo, J., Bharill, S., Papp, F., Panyi, G., Stühmer, W., Isacoff, E.Y., and Pardo, L.A. (2017). A new mechanism of voltage-dependent gating exposed by K_V10.1 channels interrupted between voltage sensor and pore. *J Gen Physiol.* 149**,** 577-593. doi: 10.1085/jgp.201611742

Toplak, Z., Hendrickx, L.A., Abdelaziz, R., Shi, X., Peigneur, S., Tomasic, T., Tytgat, J., Peterlin-Masic, L., and Pardo, L.A. (2022). Overcoming challenges of HERG potassium channel liability through rational design: Eag1 inhibitors for cancer treatment. *Med Res Rev* 42**,** 183-226. doi: 10.1002/med.21808

Tsien, R., and Pozzan, T. (1989). "[14] Measurement of cytosolic free Ca2+ with quin2," in *Methods in Enzymology*. Academic Press), 230-262.

Verkest, C., Schaefer, I., Nees, T.A., Wang, N., Jegelka, J.M., Taberner, F.J., and Lechner, S.G. (2022). Intrinsically disordered intracellular domains control key features of the mechanically-gated ion channel PIEZO2. *Nat Commun* 13**,** 1365. doi: 10.1038/s41467-022-28974-6

Wang, W., and Mackinnon, R. (2017). Cryo-EM Structure of the Open Human Ether-à-go-go -Related K + Channel hERG. *Cell* 169**,** 422-430.e410. doi: 10.1016/j.cell.2017.03.048

Wang, Z.-J., Soohoo, S.M., Tiwari, P.B., Piszczek, G., and Brelidze, T.I. (2020). Chlorpromazine binding to the PAS domains uncovers the effect of ligand modulation on EAG channel activity. *Journal of Biological Chemistry***,** jbc.RA119.012377. doi: 10.1074/jbc.RA119.012377

Whicher, J.R., and Mackinnon, R. (2016). Structure of the voltage-gated K+ channel Eag1 reveals an alternative voltage sensing mechanism. *Science* 353**,** 664-669. doi: 10.1126/science.aaf8070

Whicher, J.R., and Mackinnon, R. (2019). Regulation of Eag1 gating by its intracellular domains. *Elife* 8. doi: 10.7554/eLife.49188

Wynia-Smith, S.L., Gillian-Daniel, A.L., Satyshur, K.A., and Robertson, G.A. (2008). hERG gating microdomains defined by S6 mutagenesis and molecular modeling. *J Gen Physiol* 132**,** 507-520. doi: 10.1085/jgp.200810083

Zhao, Y., Goldschen-Ohm, M.P., Morais-Cabral, J.H., Chanda, B., and Robertson, G.A. (2017). The intrinsically liganded cyclic nucleotide–binding homology domain promotes KCNH channel activation. *The Journal of General Physiology*. doi: 10.1085/jgp.201611701

Ziechner, U., Schönherr, R., Born, A.-K., Gavrilova-Ruch, O., Glaser, R.W., Malesevic, M., Küllertz, G., and Heinemann, S.H. (2006). Inhibition of human ether à go-go potassium channels by Ca2+/calmodulin binding to the cytosolic N- and C-termini. *FEBS Journal* 273**,** 1074-1086. doi: 10.1111/j.1742-4658.2006.05134.x